Combustion noise analysis of a turbulent spray flame using a hybrid DNS/APE-RF approach

Abhishek L. Pillai[a,*], Ryoichi Kurose[a]

[a] *Department of Mechanical Engineering and Science, and Advanced Research Institute of Fluid Science and Engineering, Kyoto University, Kyoto daigaku-Katsura, Nishikyo-ku, Kyoto 615–8540, Japan*

Abstract

Combustion generated noise of a turbulent spray flame has been investigated using a hybrid Computational Fluid Dynamics/Computational Aero-Acoustics (CFD/CAA) framework. In this two-step framework, the reacting flow-field of a flame is simulated using Direct Numerical Simulations (DNS) in the first step, while the acoustic wave propagation in a non-uniform mean flow is captured by solving the Acoustic Perturbation Equations extended to Reacting Flows (APE-RF) in the second step. The numerical approach used in this study is therefore, termed as the hybrid DNS/APE-RF approach. First, this hybrid DNS/APE-RF approach is used to simulate a benchmark experimental open turbulent non-premixed flame, and the results obtained for the non-premixed flame's flow-field statistical quantities, as well as radiated sound intensities are extensively validated against experimental data. Next, the hybrid DNS/APE-RF approach is applied to an experimental open turbulent spray flame, for simulating its two-phase reacting flow-field along

*Corresponding author

Email address: pillai.abhisheklakshman.2e@kyoto-u.ac.jp (Abhishek L. Pillai)

with its combustion generated acoustic field, to predict and analyze the noise radiation behavior. The DNS results of the spray flame are compared with measurements, in terms of droplet velocity statistics and gas-phase temperatures, and favorable agreement is observed. The computed acoustic power spectra of the spray flame exhibit a power law dependence of the form $f^{-2.4}$ (where f is the frequency) in the frequency range 300 Hz $<$ f $<$ 1000 Hz. And, the computed noise spectra of the spray flame contain a nearly constant sound pressure level plateau, for frequencies greater than 1000 Hz and up to 3000 Hz. Acoustic refraction effects induced by sound speed variations in the flame, resulting in the attenuation of high-frequency noise radiated in the flame downstream direction, are also captured in the simulation. Noise radiation characteristics of the turbulent spray flame are found to resemble those of turbulent premixed and non-premixed flames.
Keywords: Combustion noise, Hybrid DNS/APE-RF approach, Turbulent spray flame, Two-phase reacting flow

1. Introduction

In a typical gas turbine engine of an aircraft, the major contributors to engine noise emission are the fan, compressor, combustor, turbine and jet exhaust. Noise from the rotating turbomachinery, i.e. fan, compressor and turbine have been suppressed to the best possible extent, owing to research and development aimed at better designs of blade geometries supplemented by potent acoustic liners. Since the 1960s, considerable amount of research efforts have been invested to study the properties and generation mechanisms of jet noise [1–4]. Then came the turbofan engines with high-bypass ratios,

and the more recent ultra-high-bypass ratio turbofan engines. The lower jet-exhaust velocities in such engines drastically attenuated the jet noise. Additionally, improvements in nozzle designs (e.g. Chevron nozzle) led to further reduction in jet-exhaust noise.

With the reduction in noise emissions from rotating turbomachinery and jet exhaust, combustion noise has emerged as a dominant contributor to engine-core noise and an issue that needs resolution, due to the stringent noise emission norms being imposed by regulatory authorities like the International Civil Aviation Organization (ICAO). To minimize the impact of burning fossil fuels in gas turbine engines on the environment, focus has now shifted towards combustor designs with low-emissions of NOx and greenhouse gases employing advanced combustion technologies, such as lean direct injection and lean premixed pre-vaporized combustion. However, such lean combustion is known to produce substantially louder noise, because of its inherently unsteady nature [5, 6]. Apart from being a major source of noise pollution which causes adverse effects on health and quality of life upon long-term exposure, combustion noise can also trigger combustion instabilities [7–9] in the gas turbine combustors, especially the ones using lean combustion strategies. Combustion instabilities are characterised by discrete tones, and accompanied by loud noise and drastic pressure fluctuations that can lead to structural damage of engine components [5, 10].

In commercial gas turbine engines as well as auxiliary power units, fuel is introduced inside the combustors in either gaseous form or as liquid spray, which then undergoes subsequent turbulent combustion resulting in heat addition in the combustors. Combustion noise is a by-product of this turbulent

combustion and for combustion occurring in confinement, such as combustion inside a gas turbine combustor, the total noise emitted is made up of direct and indirect combustion noise [11]. Direct combustion noise originates from heat release rate fluctuations associated with the interaction between turbulence and chemical reactions [11]. Direct combustion noise is perceived as the unsteady volumetric expansion and contraction of the reacting gas mixture arising from said fluctuations of heat release rate, and is a characteristic feature of open turbulent flames. Indirect combustion noise on the other hand, corresponds to the pressure perturbations generated by the acceleration of entropy and vorticity non-uniformities as they get convected through the turbine stages and nozzle beyond the combustor outlet [12–15].

Extensive experimental investigations have been performed for combustion noise generated by open turbulent premixed flames [11, 16–21] as well as open turbulent non-premixed flames [22–24]. Hirsch et al. [25] performed experimental investigations of premixed swirling jet flames and proposed a spectral model for the combustion noise from turbulent premixed combustion. Liu and Echekki [26] modelled the combustion noise spectrum of turbulent premixed V-flames by analysing DNS data. Haghiri et al. [27] performed DNS of noise generation by turbulent premixed flames. Studies utilizing numerical simulations to investigate the response of a turbulent premixed flame [28] and an acoustically excited laminar premixed flame [29, 30], to hydrodynamic instability and shear layer effect have also been conducted. While, Clavin and Siggia [31] presented a theoretical analysis of the noise emitted by turbulent premixed flames, and predicted a power law dependence ($f^{-5/2}$, f is the noise frequency) of the acoustic power spectrum by relating the noise

emission from turbulent premixed flames to the flow-field turbulence.

The relatively new class of numerical techniques called the hybrid Computational Fluid Dynamics/Computational Aero-Acoustics (CFD/CAA) strategies, have also been used as viable tools for investigating combustion noise emission from flames. In the works by Ihme et al. [32] and Ihme and Pitsch [33], the direct combustion noise generated by a turbulent non-premixed flame was investigated using a hybrid model combining Large-Eddy Simulation (LES) for the reactive flow-field, and Lighthill's acoustic analogy for the radiated acoustic field. The LES/CAA framework has also been used by Flemming et al. [34] to investigate the noise radiated from turbulent non-premixed flames, by coupling LES with two acoustic methods, viz. the Equivalent Source Method (ESM) and the Boundary Element Method (BEM). In another investigation [35], a hybrid approach combining LES for the reacting flow-field with a CAA method employing a wave equation approach (Lighthill's analogy) to solve for the propagation of acoustic waves, was used to study the combustion noise in a turbulent non-premixed flame. There also exist studies using the Random Particle Mesh for Combustion Noise (RPM-CN) method [36, 37], which is a hybrid Reynolds-averaged Navier-Stokes (RANS)/CAA approach for simulation of combustion noise from open turbulent non-premixed flames. More recently, Bui et al. [38, 39] applied the hybrid LES/APE-RF approach to analyse the combustion generated acoustic field and sound source mechanisms of turbulent non-premixed flames. In this hybrid LES/CAA approach, the acoustic wave propagation is computed by solving the Acoustic Perturbation Equations for Reacting Flows (APE-RF), which is an extension of the original system of Acoustic Perturbation

Equations (APE) developed by Ewert and Schröder [40] to multicomponent reacting flows. Schlimpert et al. [41] also applied the LES/APE approach to analyse the combustion noise from a turbulent premixed slot jet flame, and Pausch et al. [42] used the LES/CAA approach to study the acoustic response of turbulent premixed flames with round and slot burner configurations.

It is worth mentioning that, all of the above studies focus primarily on combustion noise radiation from turbulent premixed and non-premixed flames. There aren't enough numerical or experimental studies that deal with the combustion noise phenomena in turbulent spray flames/combustion in existing scientific literature. Therefore, the main objective of this work is to analyze the combustion noise characteristics of an open turbulent spray flame using a hybrid DNS/APE-RF approach. In this two-step hybrid approach, the first step involves DNS of the reactive flow-field of the turbulent flame. The DNS is restricted to the source region only, which implies that the physical size of its computational domain is sufficiently large enough to capture the near-field of the turbulent flame, within which the sources exciting acoustic waves are expected to be present. The second step involves the CAA simulation in which the APE-RF system is solved, and the acoustic wave propagation is captured all the way into the far-field. Thus, the physical size of the computational domain of CAA simulation is much larger than that of the DNS, and the CAA grid is coarser than that of the DNS. This application of separate numerical techniques specifically tailored for each simulation, is made possible by the large disparity in the characteristic fluid dynamic and acoustic length scales. Because, for low Mach number re-

acting flows, the acoustic length scales are more than an order of magnitude larger than the fluid dynamic length scales. Hence, the hybrid approach is a computationally more efficient and much cheaper alternative to performing a compressible CFD simulation of a turbulent flame, on a large computational domain that extends up to the acoustic far-field.

In this study, the hybrid DNS/APE-RF approach is first applied to a benchmark open turbulent non-premixed Hydrogen flame of the workshop for turbulent non-premixed flames (TNF-workshop) [43], designated as H3 [44]. The results for its flow-field statistical quantities obtained from the DNS as well as the combustion noise results obtained from the CAA simulation are validated against measurements. Based on this validation of the numerical framework, the hybrid DNS/APE-RF approach is used for simulating the two-phase reacting flow-field and the acoustic field of an experimental open turbulent spray flame designated as EtF3 [45]. Thus, combustion generated acoustic field of the open turbulent spray flame is predicted and characteristics of the radiated noise are investigated.

2. Direct Numerical Simulation

The DNS performed in this study employ neither any turbulence model nor any turbulence-chemistry interaction model. But, for modeling the combustion chemistry in both the turbulent non-premixed flame H3 and the spray flame EtF3, simplified reaction mechanisms (one- and two-step global reaction models, respectively) have been used which are explained later. In the DNS of turbulent spray flame, the carrier gas-phase is treated as an Eulerian continuum, and the dispersed fuel droplets are tracked as Lagrangian mass

points. For DNS of the turbulent non-premixed Hydrogen flame, there exists no dispersed-phase and hence, only the governing equation of gas-phase apply. Details of the Eulerian-Lagrangian framework are now presented.

2.1. Governing equations of gas-phase

For the gas-phase which is solved in an Eulerian framework, the governing equations for conservation of mass, momentum, energy, and species mass fraction apply as follows

$$\frac{\partial \rho}{\partial t} + \nabla \cdot (\rho \boldsymbol{u}) = S_\rho \tag{1}$$

$$\frac{\partial \rho \boldsymbol{u}}{\partial t} + \nabla \cdot (\rho \boldsymbol{u}\boldsymbol{u}) = -\nabla p + \nabla \cdot \boldsymbol{\tau} + S_{\rho u} \tag{2}$$

$$\frac{\partial \rho h}{\partial t} + \nabla \cdot (\rho h \boldsymbol{u}) = \frac{\partial p}{\partial t} + \boldsymbol{u} \cdot \nabla p + \nabla \cdot (\rho D_h \nabla h) + \boldsymbol{\tau} : \nabla \boldsymbol{u} + S_{rad} + S_{\rho h} \tag{3}$$

$$\frac{\partial \rho Y_k}{\partial t} + \nabla \cdot (\rho Y_k \boldsymbol{u}) = \nabla \cdot (\rho D_k \nabla Y_k) + S_{comb,k} + S_{\rho Y_k} \tag{4}$$

along with the equation of state for ideal gas. In Eqs. (1) - (4), ρ is the density, $\boldsymbol{u}$ is the gas-phase velocity, $\boldsymbol{\tau}$ is the stress tensor, p is the pressure, h is the specific enthalpy, and Y_k is the mass fraction of k^{th} chemical species. S_{rad} represents the source term for radiative heat loss rate per unit volume and is modeled using an optically thin approximation [46–48], and source term $S_{comb,k}$ is the mass rate of production/consumption of k^{th} species per unit volume due to combustion reaction. D_h is the gaseous thermal diffusivity and D_k is the mass diffusion coefficient of k^{th} species, respectively and are defined as

$$D_h = \frac{\lambda}{\rho c_p}, \qquad D_k = \frac{\lambda}{\rho c_p} \tag{5}$$

assuming unity Lewis number ($Le = 1$). Here λ is the thermal conductivity and c_p is the specific heat.

Furthermore, the Particle-Source-In-Cell (PSI-Cell) approach [49] is employed for achieving phase coupling between the gas-phase and dispersed-phase (fuel droplets) via. the source terms S_ρ, $S_{\rho u}$, $S_{\rho h}$, and $S_{\rho Y_k}$ in Eqs. (1) - (4), which represent the interactions between gas-phase and dispersed-phase. In the PSI-Cell approach, the computational cells are considered as control volumes and the droplets are regarded as point-sources of mass, momentum and energy to the gas-phase. When an evaporating fuel droplet passes through a computational cell (control volume), the change in it's mass, momentum and energy is considered as source (or sink) to the mass, momentum and energy of the gas-phase, respectively. Thus, two-way coupling between the gas-phase and the dispersed-phase is established using the source terms S_ρ, $S_{\rho u}$, $S_{\rho h}$, and $S_{\rho Y_k}$, which are evaluated as

$$S_\rho = -\frac{1}{\Delta V}\sum_N \frac{dm_d}{dt} \tag{6}$$

$$S_{\rho u} = -\frac{1}{\Delta V}\sum_N \frac{dm_d \boldsymbol{u}_d}{dt} \tag{7}$$

$$S_{\rho h} = -\frac{1}{\Delta V}\sum_N \frac{dm_d h_d}{dt} \tag{8}$$

$$\begin{aligned} S_{\rho Y_k} &= -\frac{1}{\Delta V}\sum_N \frac{dm_d}{dt} \quad \text{for fuel} \quad (k = F) \\ &= 0 \quad \text{for other chemical species} \ (k \neq F) \end{aligned} \tag{9}$$

Here ΔV is the volume of each control volume (each computational grid

cell) for the gas-phase calculation, m_d the fuel droplet mass, $\boldsymbol{u}_d$ the droplet velocity, h_d the specific enthalpy of a fuel droplet, and N the number of fuel droplets within a control volume. In case of the turbulent non-premixed Hydrogen flame H3, $S_\rho = S_{\rho u} = S_{\rho h} = S_{\rho Y_k} = 0$.

2.2. Governing equations of dispersed-phase (for spray flame)

A non-equilibrium Langmuir-Knudsen evaporation model [50–52] is used for capturing the evaporation phenomenon of the fuel droplets, because non-equilibrium effects are important for droplet diameters less than $d_d < 50\mu$m [51]. Secondary atomization, collisions and dense particulate effects of droplets are neglected, since the volumetric loading of droplets in the dilute spray flame considered in this study is small (droplet volume fraction $\approx 4.6 \times 10^{-4}$). The evaporating fuel droplets of the dispersed-phase are tracked individually using a Lagrangian framework [48, 50–53] by solving the equations for droplet position $\boldsymbol{x}_d$, velocity $\boldsymbol{u}_d$, temperature T_d, and mass m_d as follows.

$$\frac{d\boldsymbol{x}_d}{dt} = \boldsymbol{u}_d \tag{10}$$

$$\frac{d\boldsymbol{u}_d}{dt} = \frac{f_1}{\tau_d}(\boldsymbol{u} - \boldsymbol{u}_d) + \mathbf{g} \tag{11}$$

$$\frac{dT_d}{dt} = \left(\frac{\mathrm{Nu}}{3\mathrm{Pr}}\right)\left(\frac{c_p}{c_{p,d}}\right)\left(\frac{f_2}{\tau_d}\right)(T - T_d) + \frac{1}{m_d}\left(\frac{dm_d}{dt}\right)\frac{L_V}{c_{p,d}} \tag{12}$$

$$\frac{dm_d}{dt} = -\left(\frac{\mathrm{Sh}}{3\mathrm{Sc}}\right)\frac{m_d}{\tau_d}\ln(1 + B_M) \tag{13}$$

Here, T is the gas-phase temperature, c_p is the specific heat of gas mixture, $c_{p,d}$ is the specific heat of fuel droplet, and $\mathbf{g}$ is the gravitational acceleration.

The latent heat of vaporization L_V at T_d is given by

$$L_V = L_{V,T_{BL,atm}} \left(\frac{T_{CL} - T_d}{T_{CL} - T_{BL,atm}} \right)^{0.38} \tag{14}$$

where, $L_{V,T_{BL,atm}}$ is the latent heat of vaporization at atmospheric pressure, T_{CL} is the critical temperature of fuel, and $T_{BL,atm}$ is the boiling point of fuel at atmospheric pressure. The droplet response time τ_d, which represents the time needed for the droplet velocity to adapt to its surrounding gas-phase flow velocity is calculated as

$$\tau_d = \frac{\rho_d {d_d}^2}{18\mu} \tag{15}$$

where, d_d is the droplet diameter, ρ_d is the fuel droplet density and μ is the gas-phase dynamic viscosity. The gas-phase Prandtl and Schmidt numbers are defined as

$$\mathrm{Pr} = \frac{\mu c_p}{\lambda}, \qquad \mathrm{Sc} = \frac{\mu}{\rho D_k} \tag{16}$$

respectively. The Nusselt and Sherwood numbers are given by

$$\mathrm{Nu} = 2 + 0.552 {\mathrm{Re}_{\mathrm{sl}}}^{1/2} \mathrm{Pr}^{1/3}, \qquad \mathrm{Sh} = 2 + 0.552 {\mathrm{Re}_{\mathrm{sl}}}^{1/2} \mathrm{Sc}^{1/3} \tag{17}$$

respectively. Here, $\mathrm{Re}_{\mathrm{sl}}$ is the droplet Reynolds number based on the slip velocity $U_{sl} = |\boldsymbol{u} - \boldsymbol{u}_d|$ and given by

$$\mathrm{Re}_{\mathrm{sl}} = \frac{\rho U_{sl} d_d}{\mu} \tag{18}$$

B_M in Eq. (13) is the Spalding mass transfer number evaluated as

$$B_M = \frac{Y_{F,s} - Y_F}{1 - Y_{F,s}} \tag{19}$$

Where, Y_F is the mass fraction of fuel vapour on the far-field condition for the droplets (the same condition is used for u_i and T), and $Y_{F,s}$ is the fuel vapour mass fraction on the droplet surface calculated as follows

$$Y_{F,s} = \frac{X_{F,s}}{X_{F,s} + (1 - X_{F,s})W_{avg}/W_F} \tag{20}$$

$$X_{F,s} = \frac{p_{sat}}{p} - \left(\frac{2L_k}{d_d}\right)\beta \tag{21}$$

Here, W_{avg} is the averaged molecular weight of mixture gas, W_F is the molecular weight of the fuel vapour, p_{sat} is the saturated vapour pressure, and $X_{F,s}$ is the fuel vapour mole fraction at the droplet surface for which the non-equilibrium effects are accounted for using the Langmuir-Knudsen evaporation law [50, 51, 54]. Furthermore, L_K and β in Eq. (21) are the Knudsen layer thickness and the non-dimensional evaporation parameter, respectively and are computed as follows

$$L_k = \frac{\mu[2\pi T_d(R/W_F)^{(1/2)}]}{\mathrm{Sc}\ p} \tag{22}$$

$$\beta = -\left(\frac{\rho_d \mathrm{Pr}}{8\mu}\right)\frac{dd_d{}^2}{dt} \tag{23}$$

Here, R is the universal gas constant (R = 8.314 J/mol K). In Eqs. (11) and (12), f_1 and f_2 are the corrections to Stokes drag and heat transfer for

evaporating fuel droplets, respectively [51, 55–57] and are evaluated as

$$f_1 = \frac{1 + 0.0545\mathrm{Re_{sl}} + 0.1{\mathrm{Re_{sl}}}^{1/2}(1 - 0.03\mathrm{Re_{sl}})}{1 + b|\ \mathrm{Re}_b\ |^c} \tag{24}$$

$$b = 0.06 + 0.077\exp(-0.4\mathrm{Re_{sl}}) \tag{24a}$$

$$c = 0.4 + 0.77\exp(-0.04\mathrm{Re_{sl}}) \tag{24b}$$

$$f_2 = \frac{\beta}{e^{\beta} - 1} \tag{25}$$

where, Re_b is the droplet Reynolds number based on the blowing velocity U_b given by

$$\mathrm{Re}_b = \frac{\rho U_b d_d}{\mu}, \qquad U_b = \frac{1}{(\pi {d_d}^2 \rho)} \frac{dm_d}{dt} \tag{26}$$

2.3. Reaction models

The simulations performed in this study are referred to as Direct Numerical Simulations in the sense that, governing equations (1) - (4) are solved without using a turbulence model nor a turbulence-chemistry interaction model. However, the combustion of fuel in both flames are modeled using reduced chemistry, which is explained next. In this study, one- and two-step global reaction models are used instead of detailed chemistry for the combustion reactions. This is done in order to keep the computational turnaround times realizable, and moreover, for capturing the physics of interest in the present study, simplified reaction mechanisms will suffice [27, 58, 59]. The simplified reaction models used in this study were constructed by modifying the parameters of the reaction rates, such that they yield good predictions of experimentally measured flame speeds and temperatures over a wide range

of equivalence ratios [60, 61]. There are many previous numerical studies on turbulent combustion [53, 62–67] where DNS has been performed in conjunction with reduced reaction mechanisms (one- or two-step global reaction models).

2.3.1. Reaction model for non-premixed Hydrogen flame H3

The term $S_{comb,k}$, appearing on the right hand side of Eq. (4) represents the reaction source term for the k^{th} species. For the non-premixed Hydrogen flame, the combustion reaction of Hydrogen is described using a one-step global reaction model [60] as shown below with 4 species (H_2, O_2, H_2O and N_2).

$$H_2 + \frac{1}{2}O_2 \overset{k_{global}}{\rightarrow} H_2O \tag{27}$$

And, $S_{comb,k}$ is evaluated as

$$S_{comb,k} = -\frac{n_k}{n_F} W_k k_{global} \tag{28}$$

Here, n_k and n_F are the molar stoichiometric coefficients of the k^{th} species and fuel, respectively, and W_k is the molecular weight of the k^{th} species. k_{global} is the reaction rate of the one-step global reaction expressed by an Arrhenius formation as follows

$$k_{global} = 1.8 \times 10^{13} \exp\left(\frac{-17614}{T}\right) [H_2]^{1.0} [O_2]^{0.5} \tag{29}$$

2.3.2. Reaction model for Ethanol spray flame EtF3

The liquid spray fuel of the turbulent flame under investigation is Ethanol (C_2H_5OH). For describing the combustion reaction of gaseous Ethanol, a two-step global reaction mechanism [61] with 6 species (C_2H_5OH, O_2, CO_2, H_2O, N_2 and CO) is used as the reaction model. This reaction model was constructed by optimizing the reaction rate parameters [61] to achieve good predictions of flame speeds (for a wide range of equivalence ratios), rich and lean flammability limits, flame temperature, and burned gas composition. The two-step global reaction is as follows

$$C_2H_5OH + 2O_2 \xrightarrow{k_1} 2CO + 3H_2O \tag{30}$$

$$CO + \frac{1}{2}O_2 \underset{k_{-2}}{\overset{k_2}{\rightleftarrows}} CO_2 \tag{31}$$

Here, k_1 is the rate of Ethanol oxidation in Eq. (30) and k_2 is the rate of forward reaction for CO oxidation in Eq. (31). The reaction rates are expressed as modified Arrhenius formulations [61] given below.

$$k_1 = 1.8 \times 10^{12} \exp\left(\frac{-30}{RT}\right) [C_2H_5OH]^{0.15}[O_2]^{1.6} \tag{32}$$

$$k_2 = 10^{14.6} \exp\left(\frac{-40}{RT}\right) [CO]^1[H_2O]^{0.5}[O_2]^{0.25} \tag{33}$$

And, the reverse reaction in Eq. (31) has a rate k_{-2} that is defined according to [61]

$$k_{-2} = 5 \times 10^8 \exp\left(\frac{-40}{RT}\right) [CO_2]^1 \tag{34}$$

The terms in square brackets in Eqs. (29), (32) - (34) are the molar concentrations (moles/m^3) of different chemical species. The molar concentration $[X_k]$ of k^{th} species is, $[X_k] = [\rho Y_k / W_k]$. The two-step global reaction model used in this study for Ethanol combustion gives a more accurate estimate of flame parameters compared to a one-step global reaction model [61].

3. Acoustic Perturbation Equations for Reacting Flows (APE-RF)

Ewert and Schröder [40] formulated the system of homogeneous Acoustic Perturbation Equations (APE) and simulated the trailing edge noise from an airfoil using the hybrid LES/APE approach [68]. Later, Bui et al. [38, 39] extended the APE system to multicomponent reacting flows (APE-RF) to simulate combustion generated noise due to its ability to capture wave propagation in non-uniform mean flows with varying mean speed of sound (acoustic refraction and convection effects are considered), while preventing excitation of instabilities. The APE-RF system is expressed as

$$\frac{\partial \rho'}{\partial t} + \nabla \cdot (\rho' \overline{\boldsymbol{u}} + \overline{\rho} \boldsymbol{u'}) = q_{c,rf} \tag{35}$$

$$\frac{\partial \boldsymbol{u'}}{\partial t} + \nabla (\overline{\boldsymbol{u}} \cdot \boldsymbol{u'}) + \nabla \left(\frac{p'}{\overline{\rho}} \right) = \boldsymbol{q}_{m,rf} \tag{36}$$

$$\frac{\partial p'}{\partial t} - \overline{c}^2 \frac{\partial \rho'}{\partial t} = q_{e,rf} \tag{37}$$

In Eqs. (35) - (37) the density ρ, velocity $\boldsymbol{u}$ and pressure p have been decomposed into time averaged mean ($\overline{\rho}$, $\overline{\boldsymbol{u}}$ and $\overline{p}$, denoted by an overbar) and fluctuating (ρ', $\boldsymbol{u'}$ and p', denoted by a prime) parts as $\rho = \overline{\rho} + \rho'$, $\boldsymbol{u} = \overline{\boldsymbol{u}} + \boldsymbol{u'}$, and $p = \overline{p} + p'$. While, $\overline{c}$ is the mean speed of sound, and $q_{c,rf}$,

$\boldsymbol{q}_{m,rf}$ and $q_{e,rf}$ are the acoustic source terms for the equations governing perturbation density, velocity and the pressure-density relation, respectively. These source terms are computed from the DNS and given by

$$q_{c,rf} = -\nabla \cdot (\rho' \boldsymbol{u'})' \tag{38}$$

$$\begin{aligned}\boldsymbol{q}_{m,rf} = \nabla p \left(\frac{1}{\overline{\rho}} - \frac{1}{\rho}\right) - \frac{1}{\overline{\rho}} \left[\nabla \overline{p} + \left(\frac{\rho}{\overline{\rho}} c^2 - \overline{c}^2\right) \nabla \overline{\rho}\right] \\ + \left[\frac{\nabla \cdot \boldsymbol{\tau}}{\rho} + \sum_n Y_k f_k - (\overline{\boldsymbol{u}} \cdot \nabla)\overline{\boldsymbol{u}} - (\boldsymbol{u'} \cdot \nabla)\boldsymbol{u'} - (\boldsymbol{\omega'} \times \overline{\boldsymbol{u}}) - (\overline{\boldsymbol{\omega}} \times \boldsymbol{u'})\right]\end{aligned} \tag{39}$$

$$\begin{aligned}q_{e,rf} = -\overline{c}^2 \Bigg[\left(\frac{\overline{\rho}}{\rho} + \frac{p - \overline{p}}{\rho \overline{c}^2}\right) \frac{D\rho}{Dt} - \frac{1}{\overline{c}^2} \frac{Dp}{Dt} - \nabla \cdot (\boldsymbol{u} \rho_e) \\ \underbrace{- \frac{\gamma - 1}{\gamma} \boldsymbol{u} \cdot \nabla \overline{\rho} - \frac{p}{\overline{c}^2} \boldsymbol{u} \cdot \left(\frac{\nabla \overline{p}}{\overline{p}} - \frac{\nabla \overline{\rho}}{\overline{\rho}}\right)}_{\chi} \Bigg]\end{aligned} \tag{40}$$

In Eq. (39), which defines the source term $\boldsymbol{q}_{m,rf}$ of the perturbation velocity Eq. (36), Y_k and f_k are the mass fraction of species k and the volume force acting on species k, respectively, while $\boldsymbol{\omega'} = \nabla \times \boldsymbol{u'}$ and $\overline{\boldsymbol{\omega}} = \nabla \times \overline{\boldsymbol{u}}$.

In Eq. (40) for the source term $q_{e,rf}$ of the pressure-density relation in Eq. (37), γ is the ratio of specific heats, ρ_e is the excess density [69] defined as

$$\rho_e = (\rho - \overline{\rho}) - \frac{p - \overline{p}}{\overline{c}^2} \tag{41}$$

The term $q_{e,rf}$ contains various source mechanisms that excite acoustic waves

in combustion generated noise. The first term of $q_{e,rf}$ i.e., the one with substantial time derivative of density $D\rho/Dt$ implicitly takes into account the effects of heat release rate per unit volume, volumetric expansion due to non-isomolar combustion, species diffusion, heat diffusion as well as viscous effects. Complete description of these source mechanisms is provided in [38, 39].

Apart from the substantial time derivative of density term $D\rho/Dt$ which includes the dominant source mechanism of combustion noise (i.e. the effect of unsteady heat release rate), there are additional source mechanisms in Eq. (40) that excite acoustic waves. Such as, χ which accounts for the effects of non-uniform mean flow, Dp/Dt term which describes excitation of acoustic waves due to combustion at non-constant pressure, and the $\nabla\cdot(\boldsymbol{u}\rho_e)$ term which describes the effect of acceleration of density inhomogeneties on the radiated acoustic field in regions where the density and speed of sound differ from ambient values [70]. The APE-RF system was derived from the conservation equations of mass, momentum and energy for multicomponent reacting flows and the detailed derivation is available in [70].

Now, the source term $\boldsymbol{q}_{m,rf}$ would be the dominant acoustic source in case of non-reacting flows as pointed out by Ewert and Schröder [40, 68, 71]. In their investigations on vortex sound problems in non-reacting flows [40, 68], the quantity $(\boldsymbol{\omega'}\times\overline{\boldsymbol{u}}+\overline{\boldsymbol{\omega}}\times\boldsymbol{u'})$ appearing in Eq. (39) which represents a perturbed form of the Lamb vector $\boldsymbol{L}=(\boldsymbol{\omega}\times\boldsymbol{u})'$, was found to be the major acoustic source. However, when low Mach number open turbulent flames with round burner configurations (such as both the flames in this investigation) are considered, the effect of unsteady chemical reaction rate

and hence, the unsteady heat release dominates over vortex generated noise [16, 24, 32, 33, 38, 70, 72]. During the simulation runs for both the spray and non-premixed flames, it was found that $q_{c,rf}$ is almost five orders of magnitude smaller than $q_{e,rf}$, and $\boldsymbol{q}_{m,rf}$ is up to two orders of magnitude smaller than $q_{e,rf}$. This is illustrated in Fig. 1, which shows the instantaneous distributions of all the acoustic source terms ($q_{c,rf}$, $\boldsymbol{q}_{m,rf}$ and $q_{e,rf}$) for the spray flame EtF3 (source term distributions for the H3 flame are not shown here because, the trends are similar and for the sake of brevity). Therefore, $q_{c,rf}$ and $\boldsymbol{q}_{m,rf}$ are assumed to be negligible in comparison to $q_{e,rf}$. The spray flame EtF3 was generated using a piloted spray burner [45], and details of its configuration are provided in Section 4.2 and Fig. 2(b). It can be seen in Fig. 1 that, the source term $\boldsymbol{q}_{m,rf}$ is situated primarily in the shear layer regions of the flame. Discussion regarding the source term $q_{e,rf}$ for both the flames is provided in Section 6.2 later. The expression for source term $q_{e,rf}$ on the RHS of pressure-density relation Eq. (37) is slightly different for a two-phase reacting flow like the spray flame, and is given by

$$\begin{aligned} q_{e,rf} = -\overline{c}^2 \Bigg[& \left(\frac{\overline{\rho}}{\rho} + \frac{p - \overline{p}}{\rho \overline{c}^2} \right) \frac{D\rho}{Dt} - \frac{1}{\overline{c}^2} \frac{Dp}{Dt} - \nabla \cdot (\boldsymbol{u} \rho_e) - \frac{\gamma - 1}{\gamma} \boldsymbol{u} \cdot \nabla \overline{\rho} \\ & - \frac{p}{\overline{c}^2} \boldsymbol{u} \cdot \left(\frac{\nabla \overline{p}}{\overline{p}} - \frac{\nabla \overline{\rho}}{\overline{\rho}} \right) + \underbrace{\frac{\rho_e}{\rho} S_\rho} \Bigg] \end{aligned} \tag{42}$$

with the additional term $(\rho_e/\rho)S_\rho$ (in underbrace) which accounts for the contribution of evaporation source term S_ρ appearing in Eq. (1). $q_{e,rf}$ is evaluated using the quantities that are obtained from the solution of DNS. As mentioned previously, the substantial time rate of change of density term in

$q_{e,rf}$ implicitly takes into account the dominant combustion noise mechanism i.e. the unsteady heat release rate along with additional source mechanisms, and for the spray combustion case the effect of energy exchange between gas-phase and dispersed-phase, i.e. the contribution of $S_{\rho h}$ term in Eq. (3) is also included in the substantial time derivative of density. This is because, the $D\rho/Dt$ term can be expressed using the energy equation for reacting flows [70, 73]. Derivation of the expression for $q_{e,rf}$ in Eq. (42) for two-phase reacting flows is described later.

In the simulations conducted by Bui et al. [38, 39] for combustion noise in open turbulent non-premixed flames, the source terms $q_{c,rf}$ and $\boldsymbol{q}_{m,rf}$ in Eqs. (35) and (36), respectively, were neglected and simplified formulations of the source term $q_{e,rf}$ were used for solving the APE-RF system. One of the reasons for this is that, it is quite cumbersome and computationally expensive to compute all the acoustic source mechanisms in the APE-RF system. The simplified formulations of $q_{e,rf}$ retained the major source mechanism i.e., the $D\rho/Dt$ term which contains the unsteady heat release rate effect. And it was found that this simplified formulation of $q_{e,rf}$ was sufficient to obtain good predictions of the combustion generated acoustic fields, as the influence of neglected terms on the acoustic fields was insignificant.

However, in this study the full expressions of $q_{e,rf}$ as given in Eqs. (40) and (42) for the non-premixed and spray flames, respectively are employed. This is necessary because, unlike the LES of Bui et al. [38] which was performed using an incompressible code, the DNS of the flames in this investigation are performed using a compressible solver. So, if $q_{e,rf}$ is evaluated using input data from a compressible CFD simulation, it is imperative that

the full expression of $q_{e,rf}$ be used. Otherwise, using the simplified version of $q_{e,rf}$ can lead to the generation of spurious acoustic-acoustic excitations [40, 74] in the CAA simulation. It is worth mentioning that in case of the spray flame EtF3, for the source term $q_{e,rf}$ which is computed in the DNS step using the full expression as given by Eq. (42), the term $(\rho_e/\rho)S_\rho$ which incorporates the effect of density variations caused by fuel droplet evaporation, is approximately two orders of magnitude smaller than the dominant acoustic source mechanism represented by the substantial time derivative of density term $\left(\frac{\overline{\rho}}{\rho} + \frac{p-\overline{p}}{\rho\overline{c}^2}\right)\frac{D\rho}{Dt}$.

3.1. Derivation of source term $q_{e,rf}$ for two-phase reacting flows

The derivation for source term $q_{e,rf}$ in the pressure-density relation of the two-phase reacting flow (spray flame case) is now presented. Starting with the definition of excess density ρ_e as introduced by Crighton et al. [69]

$$\rho_e = (\rho - \overline{\rho}) - \frac{p - \overline{p}}{\overline{c}^2} \tag{43}$$

Taking the total time derivative of ρ_e

$$\begin{aligned} \frac{D\rho_e}{Dt} &= \frac{\partial \rho_e}{\partial t} + \boldsymbol{u} \cdot \nabla \rho_e \\ &= \frac{\partial \rho_e}{\partial t} + \nabla \cdot (\boldsymbol{u}\rho_e) - \rho_e \nabla \cdot \boldsymbol{u} \end{aligned} \tag{44}$$

The continuity equation (1) can be rewritten as

$$\frac{D\rho}{Dt} + \rho \nabla \cdot \boldsymbol{u} = S_\rho \tag{45}$$

Substituting for the divergence of velocity field using the above equation

$$\frac{D\rho_e}{Dt} = \frac{\partial \rho_e}{\partial t} + \nabla \cdot (\boldsymbol{u}\rho_e) - \frac{\rho_e}{\rho}\left(S_\rho - \frac{D\rho}{Dt}\right) \tag{46}$$

$$\begin{aligned} \frac{\partial \rho_e}{\partial t} &= \frac{D\rho_e}{Dt} - \nabla \cdot (\boldsymbol{u}\rho_e) + \frac{\rho_e}{\rho}\left(S_\rho - \frac{D\rho}{Dt}\right) \\ &= \frac{D\rho_e}{Dt} - \nabla \cdot (\boldsymbol{u}\rho_e) - \frac{\rho_e}{\rho}\frac{D\rho}{Dt} + \frac{\rho_e}{\rho}S_\rho \end{aligned} \tag{47}$$

Substituting the definition of ρ_e in the above equation

$$\begin{aligned} \frac{\partial \rho_e}{\partial t} &= \frac{D}{Dt}(\rho - \overline{\rho}) - \frac{D}{Dt}\left(\frac{p - \overline{p}}{\overline{c}^2}\right) - \nabla \cdot (\boldsymbol{u}\rho_e) + \frac{\rho_e}{\rho}S_\rho \\ &\quad - \frac{1}{\rho}\left(\rho - \overline{\rho} - \frac{p - \overline{p}}{\overline{c}^2}\right)\frac{D\rho}{Dt} \\ &= \left(\frac{\overline{\rho}}{\rho} + \frac{p - \overline{p}}{\rho\overline{c}^2}\right)\frac{D\rho}{Dt} - \frac{D\overline{\rho}}{Dt} - \nabla \cdot (\boldsymbol{u}\rho_e) - \frac{D}{Dt}\left(\frac{p - \overline{p}}{\overline{c}^2}\right) + \frac{\rho_e}{\rho}S_\rho \end{aligned} \tag{48}$$

In the above equation, local time derivatives of mean quantities will vanish (e.g. $\partial\overline{\rho}/\partial t = 0$), hence by expanding the $(D\overline{\rho}/Dt)$ term we get

$$\frac{\partial \rho_e}{\partial t} = \left(\frac{\overline{\rho}}{\rho} + \frac{p - \overline{p}}{\rho\overline{c}^2}\right)\frac{D\rho}{Dt} - \boldsymbol{u} \cdot \nabla\overline{\rho} - \nabla \cdot (\boldsymbol{u}\rho_e) - \frac{D}{Dt}\left(\frac{p - \overline{p}}{\overline{c}^2}\right) + \frac{\rho_e}{\rho}S_\rho \tag{49}$$

Therefore, using Eq. (49) the pressure-density relation of the APE-RF system for two-phase reacting flows reads

$$\frac{\partial p'}{\partial t} - \overline{c}^2\frac{\partial \rho'}{\partial t} = -\overline{c}^2\frac{\partial \rho_e}{\partial t} \tag{50}$$

$$\frac{\partial p'}{\partial t} - \overline{c}^2 \frac{\partial \rho'}{\partial t} = -\overline{c}^2 \left[\left(\frac{\overline{\rho}}{\rho} + \frac{p - \overline{p}}{\rho \overline{c}^2} \right) \frac{D\rho}{Dt} - \boldsymbol{u} \cdot \nabla \overline{\rho} - \nabla \cdot (\boldsymbol{u} \rho_e) - \frac{D}{Dt} \left(\frac{p - \overline{p}}{\overline{c}^2} \right) + \frac{\rho_e}{\rho} S_\rho \right] \tag{51}$$

With the source term $q_{e,rf}$ for two-phase reacting flow as

$$q_{e,rf} = -\overline{c}^2 \left[\left(\frac{\overline{\rho}}{\rho} + \frac{p - \overline{p}}{\rho \overline{c}^2} \right) \frac{D\rho}{Dt} - \boldsymbol{u} \cdot \nabla \overline{\rho} - \nabla \cdot (\boldsymbol{u} \rho_e) - \frac{D}{Dt} \left(\frac{p - \overline{p}}{\overline{c}^2} \right) + \frac{\rho_e}{\rho} S_\rho \right] \tag{52}$$

Upon expanding the penultimate term on the right-hand side of the above equation, the complete formulation of $q_{e,rf}$ similar to the one derived by Bui et al. [70] can be obtained

$$\begin{aligned} q_{e,rf} &= -\overline{c}^2 \left[\left(\frac{\overline{\rho}}{\rho} + \frac{p - \overline{p}}{\rho \overline{c}^2} \right) \frac{D\rho}{Dt} - \boldsymbol{u} \cdot \nabla \overline{\rho} - \nabla \cdot (\boldsymbol{u} \rho_e) \right. \\ &\quad \left. - \frac{D}{Dt} \left(\frac{p}{\overline{c}^2} \right) + \frac{D}{Dt} \left(\frac{\overline{p}}{\overline{c}^2} \right) + \frac{\rho_e}{\rho} S_\rho \right] \\ &= -\overline{c}^2 \left[\left(\frac{\overline{\rho}}{\rho} + \frac{p - \overline{p}}{\rho \overline{c}^2} \right) \frac{D\rho}{Dt} - \boldsymbol{u} \cdot \nabla \overline{\rho} - \nabla \cdot (\boldsymbol{u} \rho_e) \right. \\ &\quad \left. - \frac{1}{\overline{c}^2} \frac{Dp}{Dt} - \frac{p}{\overline{c}^2} \boldsymbol{u} \cdot \left(\frac{\nabla \overline{p}}{\overline{p}} - \frac{\nabla \overline{\rho}}{\overline{\rho}} \right) + \frac{D}{Dt} \left(\frac{\overline{p}}{\gamma \overline{p} / \overline{\rho}} \right) + \frac{\rho_e}{\rho} S_\rho \right] \end{aligned} \tag{53}$$

Since, the local time derivatives of time averaged mean variables are zero

$$q_{e,rf} = -\overline{c}^2 \left[\left(\frac{\overline{\rho}}{\rho} + \frac{p - \overline{p}}{\rho \overline{c}^2} \right) \frac{D\rho}{Dt} - \nabla \cdot (\boldsymbol{u} \rho_e) - \boldsymbol{u} \cdot \nabla \overline{\rho} - \frac{1}{\overline{c}^2} \frac{Dp}{Dt} - \frac{p}{\overline{c}^2} \boldsymbol{u} \cdot \left(\frac{\nabla \overline{p}}{\overline{p}} - \frac{\nabla \overline{\rho}}{\overline{\rho}} \right) + \frac{1}{\gamma} \boldsymbol{u} \cdot \nabla \overline{\rho} + \frac{\rho_e}{\rho} S_\rho \right] \tag{54}$$

Therefore, the complete expression of source term $q_{e,rf}$ for two-phase reacting flow is

$$q_{e,rf} = -\overline{c}^2 \left[\left(\frac{\overline{\rho}}{\rho} + \frac{p - \overline{p}}{\rho \overline{c}^2} \right) \frac{D\rho}{Dt} - \nabla \cdot (\boldsymbol{u} \rho_e) - \frac{\gamma - 1}{\gamma} \boldsymbol{u} \cdot \nabla \overline{\rho} - \frac{1}{\overline{c}^2} \frac{Dp}{Dt} \right. \\ \left. - \frac{p}{\overline{c}^2} \boldsymbol{u} \cdot \left(\frac{\nabla \overline{p}}{\overline{p}} - \frac{\nabla \overline{\rho}}{\overline{\rho}} \right) + \frac{\rho_e}{\rho} S_\rho \right] \tag{55}$$

4. Computational setup

4.1. Turbulent non-premixed flame H3

The turbulent non-premixed flame simulated in this study is a benchmark flame of the workshop for turbulent non-premixed flames [43], and was investigated in an experiment [44] with the designation H3. The burner configuration for this experiment consists of a 35 cm long circular stainless steel tube of diameter $D_{H3} = 8$ mm with a thinned rim at the exit. Through this tube, a mixture Hydrogen and Nitrogen gas issues out into a low velocity laminar coflow of dry air. The DNS of H3 flame is performed on a non-uniform staggered Cartesian grid consisting of $1080 \times 400 \times 400$ grid points (a total of 0.17 billion grid points) in the x-, y- and z- directions, respectively. The minimum grid size used is $\Delta x = \Delta y = \Delta z = 80$ μm. The computational domain has physical size of $106D_{H3} \times 59D_{H3} \times 59D_{H3}$ in the x-, y- and z- directions, respectively. H3 flame's parameters are summarized in Table 1, here the jet exit Mach number is defined with respect to speed of sound in ambient air c_∞. A schematic of the computational domain used for the DNS of the non-premixed Hydrogen flame H3 is illustrated in Fig. 2(a), showing the domain size and configuration of the burner's exit used as inflow boundary conditions in the DNS.

Table 1: Parameters of turbulent non-premixed flame (H3).

Flame designation	H3
Fuel (Vol %)	H_2/N_2 : 50/50
Jet diameter, D_{H3} [mm]	8
Bulk jet velocity, U_{jet} [m/s]	34.8
Coflow velocity, U_{coflow} [m/s]	0.2
Kinematic viscosity, ν [m^2/s]	2.787×10^{-5}
Jet Reynolds number, $Re = (U_{jet} D_{H3})/\nu$ [–]	10000
Jet Mach number, $M = U_{jet}/c_\infty$ [–]	0.1
Ambient temperature [K]	300

4.2. Turbulent spray flame EtF3

The open turbulent Ethanol spray flame examined in this study is designated as EtF3, and belongs to the series of Ethanol spray flames which were experimentally investigated at the University of Sydney by Gounder et al. [45], using a laboratory scale piloted spray burner. The burner configuration for this flame consists of a central jet nozzle through which fuel spray and carrier air issue out. The central jet nozzle is surrounded by a coaxial pilot annulus and an outer stream of primary co-flowing air, and the entire co-flow/burner assembly is mounted in a vertical wind tunnel that supplies a secondary co-flow of air at the same velocity as the primary air co-flow [45]. The burner and primary co-flow's exit plane is situated 59 mm downstream of the exit plane of the wind tunnel. Ethanol spray flame's parameters measured at the burner exit for the central jet nozzle are listed in Table 2, while those for the annular pilot flame are listed in Table 3. At the burner exit, the pilot consists of fully-burned product of the stoichiometric mixture of 5.08% Acetylene (C_2H_2), 10.17% Hydrogen (H_2) and 84.75% air by volume, with an

Table 2: Flow parameters of the central jet of spray flame at burner exit.

Flame designation	EtF3
Fuel	Ethanol
Jet diameter, D_{EtF3} [mm]	10.5
Bulk jet velocity, U_{jet} [m/s]	24
Bulk velocity co-flow stream, U_{coflow} [m/s]	4.5
Carrier air mass flow rate [g/min]	150
Liquid fuel injection rate [g/min]	45
Measured liquid flow at exit [g/min]	30.7
Vapour fuel flow rate at exit [g/min]	14.3
Kinematic viscosity, ν [m^2/s]	1.279×10^{-5}
Jet Reynolds number, $Re = (U_{jet} D_{EtF3})/\nu$ [–]	19,700
Jet Mach number, M $= U_{jet}/c_\infty$ [–]	0.07
Equivalence ratio at jet exit, ϕ_{exit} [–]	0.85
Initial droplet & ambient temperature [K]	293.15

adiabatic flame temperature of 2493 K. This implies that pilot flame solely consists of the chemical species CO_2, H_2O and N_2 at the burner exit, whose respective mass fractions have been calculated a priori and listed in Table 3. The pilot flame supplies the heat for evaporation of the liquid fuel droplets, ignites the vaporized Ethanol and stabilizes the main spray flame. The spray was generated using an ultrasonic nebulizer situated inside the burner about 215 mm upstream of the jet exit plane in the experiment. Among the poly-disperse droplets formed by the ultrasonic nebulizer inside the central nozzle tube, some evaporate prior to reaching the nozzle exit and that is why the measured liquid flow rate at the nozzle exit is smaller than the actual liquid fuel injection rate (see Table 2). The EtF3 spray flame burns in the partially-premixed combustion regime, and more description on the burner setup is available in [45].

Table 3: Parameters of annular pilot at burner exit.

Fuel	Acetylene (C_2H_2) + Hydrogen (H_2) + Air
Pilot diameter [mm]	25
Bulk velocity pilot (burned), U_{pilot} [m/s]	11.6
Pilot temperature [K]	2493
Pilot composition ($Y_{CO_2} : Y_{H_2O} : Y_{N_2}$)	(0.1722 : 0.10575 : 0.722)

Fig. 2(b) depicts the schematic of the computational domain used for DNS of the spray flame EtF3, showing the domain size and configuration of the piloted spray burner's exit used as inflow boundary conditions. The DNS is performed on a non-uniform staggered Cartesian grid consisting of 1160×400×400 grid points (a total of 0.19 billion grid points) in the x-, y- and z-directions, respectively. The domain size is approximately $94D_{EtF3} \times 49D_{EtF3} \times 49D_{EtF3}$ in the x-, y- and z-directions, respectively. Fuel droplets are injected randomly (meaning the position of a droplet being injected at the inflow boundary, within the cross-sectional area of the central nozzle of the burner, is chosen randomly) in a polydisperse fashion from the central jet nozzle exit plane, with the maximum droplet size used in the DNS being 80 μm. Fuel droplet size distribution produced by the ultrasonic nebulizer in the experiment follows an approximate log-normal Probability Density Function (PDF) and hence, the best fit log-normal PDF curve to the experimental droplet size distribution data as depicted in Fig. 3, is used in the present DNS.

While performing DNS of spray combustion, the grid size has to fulfil various criteria such as, the grid size should be capable of resolving the Kol-

mogorov length scales and the flame reaction zone thickness. But, at the same time, due to the two-way coupling strategy between the gas and dispersed phases using the PSI-Cell approach [49], the grid size must ideally be 10 times larger than the droplet size in order to accurately capture the droplet evaporation dynamics [75, 76]. For the present spray flame simulation to match the experiment, the fuel droplets are injected into the computational domain in a polydisperse manner with sizes ranging up to 80 μm, which puts a constraint on how small of a grid size can be used. Using grid sizes of the same order of the droplet diameters would result in significantly erroneous predictions for droplet evaporation. Moreover, large temperature values of the order of 2493 K in the pilot region, and 1300 K and higher within the flame are found (see Fig. 13), which lead to very large values of local kinematic viscosity ν (about $10-30$ times the ambient value). Furthermore, with increasing downstream location from burner exit, the turbulent velocity fluctuations also reduce (see Fig. 11), thus leading to local turbulent Reynolds numbers Re_t in the range of $50-100$. This results in the order of Kolmogorov length scale $\eta_k \approx 111\mu$m (for $Re_t = 100$). For the DNS of spray flame EtF3, a minimum grid size of $\Delta x = \Delta y = \Delta z = 150\mu$m is used, yielding $\Delta x/\eta_k \approx 1.35$ which is still less than double the Kolmogorov scale grid spacing often used in DNS of turbulent combustion [77, 78]. Additionally, a two-step global chemistry is used as the reaction model, which requires much less spatial resolution in comparison to detailed chemistry. Therefore, the grid resolution is sufficient inside the jet flame region. However, outside the flame, a relatively coarser grid is used.

5. Numerical procedures

5.1. Numerical procedure for DNS

The flow-fields of the flames are simulated by performing DNS using the in-house hybrid CFD/CAA code called FK^3-CAA, which is a new extension of the previous in-house thermal flow analysis code FK^3 [48, 53, 79–82]. The CFD solver of this code, employs a pressure-based semi-implicit solver for compressible flows [83], whose algorithm consists of a fractional-step method. The spatial derivatives of the convective terms in the momentum equation are approximated using a 6^{th} order accurate central difference scheme, while the convective terms in the governing equations of the scalar quantities are evaluated using the WENO (Weighted Essentially Non-Oscillatory) scheme [84]. The spatial derivatives of the stress tensor terms are evaluated using a 4^{th} order central difference scheme and those of the diffusive terms are discretized by a 2^{nd} order central difference scheme. The time integration of the convective terms is performed using a 3^{rd} order explicit TVD Runge-Kutta method. Additionally, all the thermodynamic properties and transport coefficients taking temperature dependence into consideration are obtained from CHEMKIN [85, 86].

5.1.1. Boundary conditions for non-premixed flame H3

For the velocity inflow condition in case of the turbulent non-premixed Hydrogen flame H3, transient turbulent velocity fluctuations generated using a digital filter based technique [87, 88] are superimposed on a fully developed turbulent pipe flow velocity profile at the nozzle exit. Outside the nozzle region in the inflow plane, the radial and azimuthal velocities are set to

zero, the axial coflow velocity of 0.2 m/s is imposed, and Neumann condition is applied for other quantities. At the outflow and lateral boundaries, the Neumann condition is imposed for all quantities. To minimize the amplitude of spurious waves reflected at the boundaries of the computational domain, a sponge zone combining grid stretching and Laplacian filtering [89] is used in the outflow direction (to dissipate the flow fluctuations and acoustic waves before they reach the outflow boundary) towards the outflow boundary, while absorbing layers consisting of grid stretching and damping terms (artificial dissipation through filtering) are implemented for the lateral boundaries of the computational domain.

5.1.2. Boundary conditions for spray flame EtF3

In case of the turbulent spray flame EtF3, radial profiles of mean axial velocity of the gas-phase and droplets in different size ranges (e.g., 1-10 μm, 10-20 μm, 20-30 μm, etc.) [45], are used as inflow boundary conditions in the DNS. In the expermient, these radial profiles of mean axial velocity were measured close to the central jet nozzle's exit plane at $x/D = 0.3$. It is also assumed that the radial profile of mean axial velocity for the smallest droplet size range ($1\mu\text{m} \leq d_d \leq 10\mu\text{m}$) corresponds to that of the gas-phase, and this assumption is in accordance with the experiment [45]. Furthermore, these mean velocity profiles represent fully developed two-phase flow behavior [45].

Additionally, for the central spray nozzle transient turbulent velocity fluctuations generated using a digital filter based technique [87, 88] are superimposed on the gas-phase mean velocities at the nozzle exit to simulate artificial inflow turbulence. The experimental data for the radial profile of RMS fluctuations of gas-phase axial velocity at the central nozzle exit plane, is supplied

to the artificial turbulence generator. Turbulence in the pilot is negligible [45]. For the region outside pilot annulus exit (i.e. for $r > 12.5$ mm) at the inflow plane, an axial co-flow air velocity of 4.5 m/s is imposed (see Table 2) while the other velocity components are set to zero, and Neumann condition is applied to other physical quantities. At the outflow and lateral boundaries, the Neumann condition is imposed for all physical quantities.

To minimize the amplitude of acoustic waves reflected at the boundaries of the computational domain, a sponge zone combining grid stretching and Laplacian filtering [89] is used in the far downstream region towards the outflow boundary (last 30 grid points in x-direction), to dissipate the flow fluctuations and acoustic waves before they reach the outflow boundary. Artificial damping provided by the Laplacian filter is applied progressively in the sponge zone. Also, absorbing layers comprising of grid stretching and artificial dissipation which is obtained by applying a sixth order filter [90], are implemented towards the lateral boundaries of the computational domain. This helps to damp out the outgoing acoustic waves, thereby minimizing the reflection of acoustic waves at the lateral boundaries.

5.2. Numerical procedure for CAA

For simulating the propagation of acoustic waves produced by the noise sources, the CAA solver of the FK^3-CAA code solves the system of APE-RF in Eqs. (35) - (37). The CAA solver uses the 4^{th} order Dispersion-Relation-Preserving (DRP) scheme of Tam and Webb [91] for discretization of the spatial derivatives, and a 4^{th} order 6-stage Low Dissipation and Dispersion Runge-Kutta (LDDRK) scheme [92] for temporal integration, to capture the acoustic wave propagation. To suppress spurious high-frequency waves, the

low-pass filtering method of Artificial Selective Damping (ASD) proposed by Tam and Shen [93] is applied.

The CAA computations for the non-premixed flame H3 are performed on a 3-D non-uniform Cartesian grid with $440 \times 340 \times 188$ grid points (a total of over 28 million grid points) in the x-, y- and z-directions, respectively. The domain size of the CAA grid for the H3 flame, in the respective Cartesian coordinate directions is $-12 \leq x/D_{H3} \leq 85$, $-12 \leq y/D_{H3} \leq 77$ and $-12 \leq z/D_{H3} \leq 12$.

While for the CAA simulation of the spray flame EtF3, the 3-D non-uniform Cartesian grid consists of $510 \times 335 \times 198$ grid points (a total of 33.83 million grid points approximately) in the x-, y- and z-directions, respectively. And, the physical size of the CAA computational domain for the spray flame is $-10 \leq x/D_{EtF3} \leq 73$, $-14 \leq y/D_{EtF3} \leq 60$ and $-13 \leq z/D_{EtF3} \leq 13$, respectively in each of the three Cartesian coordinate directions. Cell distributions in the x-y and y-z planes of the Cartesian mesh grid used in the CAA simulation of the spray flame, are illustrated in Fig. 4 for visualization.

The quantities required for computing the propagation of acoustic waves in the CAA simulation, namely the mean speed of sound $\overline{c}$, the mean density $\overline{\rho}$, the mean flow velocities $\overline{\boldsymbol{u}}$, and the source term $q_{e,rf}$, are obtained from the solution of the DNS of the reacting flow-fields of the turbulent flames in the first step. These quantities are then mapped onto the CAA grid from the DNS grid using a trilinear algorithm. The CAA grids for both the flames (H3 and EtF3) are capable of resolving frequencies up to $f_{max} = 12000$ Hz, assuming a minimum resolution of seven points per wavelength for the DRP scheme [93, 94] used in the CAA simulations. For the CAA computations of

the non-premixed flame H3, the time increment is $\Delta t = 5.25 \times 10^{-7}$ s, while in case of the spray flame EtF3 $\Delta t = 5 \times 10^{-7}$ s. The same time increment values are used for the time integration of the respective DNS computations of these flames. The value of Δt chosen for each flame ensures that the CFL criterion is not violated, and in order to enable a constant sampling frequency of the results, Δt values are kept constant in both flames' simulations. The acoustic Courant number lies in the range of $\mathrm{CFL}_{\mathrm{acoust}} = 0.75 - 0.8$ for the CAA simulations of both the flames, while the convective Courant numbers of the DNS are approximately $\mathrm{CFL}_{\mathrm{conv}} = 0.33$ for the non-premixed flame H3 and $\mathrm{CFL}_{\mathrm{conv}} = 0.14$ for the spray flame EtF3.

At the artificial boundaries between the inner DNS domain (source region) and the outer CAA domain, a damping zone treatment called silent embedded boundaries is introduced. Schröder and Ewert [71] derived the original formulation of the silent embedded boundaries to suppress the spurious noise generated by the sudden appearance of convecting vortical disturbances due to the truncated source region (i.e. CFD domain). Later Bui et al. [38] reformulated the silent embedded boundaries to be applicable to the pressure-density relation in the APE-RF system. Hence, in the present CAA simulations, silent embedded boundaries are used to suppress the spurious noise generated by the discontinuity in the distribution of entropy sources across the artificial boundary, and to avoid contamination of the acoustic solution. At the far-field boundaries of the CAA domain, the non-reflective radiation boundary conditions applicable to 3-D non-uniform mean flows, formulated by Bogey and Bailly [89] have been used to avoid unphysical reflections into the CAA domains. A sponge layer technique [89] has also been

implemented at the left and right boundaries (in the x-direction of the grid) of the CAA domain.

The DNS of the turbulent flames are initially run for tens of thousands of iterations to allow for flame development and computation of mean flow-field quantities. Then the CAA simulations are switched on in case of both flames, and there onwards in every iteration the DNS step is performed first followed by the CAA step. The source term $q_{e,rf}$ obtained from the DNS solution is interpolated onto the CAA grid at the end of every DNS step, to solve the APE-RF system in the CAA step. Sampling of the flow-field quantities (from DNS) as well as the fluctuating pressure and velocity signals (from CAA) are commenced there onwards by running the simulations for a physical time of 74 ms for the H3 flame and 99 ms for the EtF3 flame. For computation of the combustion noise results, the computed temporal signals are converted to the frequency domain using Fast Fourier Transform (FFT). The time period of signal extraction is divided into sections with a 50% overlap, and these sections are used for subsequent averaging of the noise spectra.

The complete CPU time required for the hybrid DNS/APE-RF computations (i.e. time for initial DNS plus time for combined DNS/CAA computations) is approximately 639000 hours for the H3 flame and 1105920 hours for the EtF3 flame, by parallel computation (using MPI parallelization with 1024 cores for the DNS, and OpenMP parallelization with 68 threads for the CAA simulation, in case of each flame) on a CRAY-XC40 supercomputer at the Academic Centre for Computing and Media Studies (ACCMS), Kyoto University (the actual time required for the computations is approximately 624 hours of real time for the H3 flame and 1080 hours of real time for the

EtF3 flame).

6. Results and discussion

6.1. Flow field results

The instantaneous temperature fields computed from the DNS are depicted in Fig. 5, showing the predicted flame structures of both the turbulent non-premixed jet flame H3 (left) and the turbulent spray flame EtF3 (right) in their respective central x-y planes. The lengths in the axial and radial directions for both flames depicted in Fig. 5 are the same, with the dimensions being in mm. The non-premixed flame H3 which is a purely gaseous flame has a jet exit Reynolds number $Re = 10000$, while the spray flame EtF3 has a jet exit Reynolds number $Re = 19700$. However, the lower Re H3 flame exhibits slightly wider spreading in the radial direction compared to the higher Re spray flame EtF3, further downstream of the burner exit. This is caused by the inflow velocity boundary conditions of the flames. The non-premixed flame H3 is a simple jet flame with bulk jet velocity at nozzle exit $U_{jet} = 34.8$ m/s and co-flow velocity $U_{coflow} = 0.2$ m/s. Whereas, the turbulent spray flame EtF3 is a piloted flame with bulk jet velocity at central nozzle exit $U_{jet} = 24$ m/s. The burner exit velocity of the coaxial annular pilot flame that surrounds the central jet nozzle is $U_{pilot} = 11.6$ m/s, and the co-flow velocity is $U_{coflow} = 4.5$ m/s. The H3 flame has a velocity ratio $U_{jet}/U_{coflow} = 174$, while the spray flame EtF3 has a velocity ratio $U_{jet}/U_{coflow} = 5.33$. This velocity ratio U_{jet}/U_{coflow} strongly influences the mixing layer growth and mass entrainment [95]. Therefore, the H3 flame which has a larger velocity ratio exhibits slightly more radial spreading (larger

flame width) compared to spray flame EtF3, and this is evident in Fig. 6 which shows the radial profiles of mean axial velocity and temperature at the downstream location of $x = 320$ mm from the burner exit for both flames. It can be seen in Fig. 6 that both the axial velocity and temperature of the spray flame EtF3, approach the coflow/ambient values earlier (around $r = 40$ mm) compared to the H3 flame. Moreover, the inflow configuration of the spray flame EtF3 is a bit more complex than that of the non-premixed flame H3, due to the presence of the annular pilot flame between the central jet stream and the co-flow stream. There is mixing between the central jet stream (containing Ethanol + Air) and the hot pilot stream (contains fully-burned products of combustion), between the pilot stream and the co-flow stream (Air), and between the central jet stream and the co-flow stream, all of which occur simultaneously. This produces more droplet dispersion with increasing downstream distance from the burner exit.

In Fig. 5, the instantaneous temperature field of the spray flame EtF3 also contains gray entities that represent the dispersed fuel droplets. These fuel droplets get convected downstream with the flow after exiting the central nozzle, and the size of the fuel droplets reduces gradually as a consequence of evaporation. The high temperature gas-phase surrounding the fuel droplets ignites the newly formed fuel vapors and promotes further combustion reaction. A steady reduction in droplet count with increasing distance from the burner exit in the downstream direction is evident, which is precisely due to the evaporation of droplets caused by the surrounding hot gas-phase. Once a droplet's diameter falls below 1 μm due to evaporation into gaseous Ethanol, it is omitted from the computation, and its remaining mass, momentum and

energy are transferred to the gas-phase (i.e. neighbouring grid points of the computational cell which contains the droplet) via. the source terms S_ρ, $S_{\rho u}$, $S_{\rho h}$, and $S_{\rho Y_k}$ in Eqs. (1) - (4).

Next, the flow-field quantities computed from the DNS of the H3 flame are validated against experimental data [43, 44] in the form of first and second order statistics. Computed radial profiles for mean and standard deviation of axial velocity and temperature are presented in Fig. 7. It should be noted that, the figures wherein any quantity expressed within triangular parentheses "<>" indicates the time averaging of that quantity. The DNS results show an overall good agreement with measurements at all stream-wise locations, for both the velocity and temperature statistics presented here. With increasing downstream location from the nozzle exit, the radial profiles of the mean and standard deviations of both axial velocity and temperature become flatter, and their corresponding magnitudes reduce gradually. Therefore, the H3 flame's spreading is accurately reproduced as is apparent from the radial distributions of axial velocity and temperature in Fig. 7. In Fig. 8, the DNS results for the radial profiles of standard deviation of radial velocity show good conformity to the experimental data at different stream-wise locations, while reasonable agreement is also observed for the computed radial profiles of mean and standard deviation of mixture fraction Z of the H3 flame, at different stream-wise locations as illustrated in Fig. 9. However, some discrepancies can be discerned in the DNS results for the H3 flame, especially in the standard deviations of axial velocity, temperature and mixture fraction. The major cause for these discrepancies is the unavailability of measurements for the turbulent inflow boundary conditions. Since, the

radial profiles of mean and standard deviation of velocities at the nozzle exit are unknown, it was not possible to prescribe the exact inflow boundary conditions in the DNS using the artificial turbulence generation technique of Klein et al. [87, 88]. Other possible reasons for the discrepancies include, the simplified reaction mechanism (one-step global reaction model) used to model hydrogen combustion, and the unity Lewis number assumption ($Le = 1$). Incorporation of differential diffusion effects in the present simulations would make the already costly computations even more expensive. Hence, the $Le = 1$ assumption has been implemented for the turbulent flames.

The DNS results for flow-field statistical quantities of the spray flame EtF3 are also validated against experimental data. Comparisons between DNS results for the radial profiles of droplet averaged axial velocity along with gas-phase mean axial velocity and experimental data are shown in Fig. 10. DNS predictions of droplet averaged axial velocity are in good agreement with experimental data while reproducing the radial dispersion of droplets accurately. From the measurements [45] close to the jet exit plane ($x/D = 0.3$), it is known that the smaller droplets have higher mean axial velocities compared to the larger ones. This is because the larger droplets which have longer response times (hence higher Stokes numbers) and higher inertia, are subjected to lower acceleration by the carrier gas-phase while traversing from the nebulizer head inside the burner, to the central nozzle's exit plane. However, at the stream-wise location of $x/D = 10$ the gas-phase axial velocity is quite similar to the droplet averaged axial velocity, because as the droplets exit the nozzle and get convected downstream, they will initially experience acceleration (regardless of size) due to the thermal expansion of the gas-

phase associated with heat release. Thus, the gas-phase is able to retain its momentum around $x/D = 10$ because of thermal expansion. At the further downstream location of $x/D = 20$, the droplet averaged axial velocity starts becoming higher than the gas-phase axial velocity for radial locations $r/D > 0.5$. This tendency occurs because, with increasing downstream distance and especially for the far downstream location of $x/D = 20$, there will be a general shift towards larger droplets among the existing ones, since the smaller droplets evaporate faster. The larger droplets with higher inertia and Stokes numbers are less responsive to changes in the local gas-phase flow. Therefore, the larger droplets retain their axial velocities as they are not subjected to the same amount of deceleration as the gas-phase.

Next, the DNS predicted radial profiles of standard deviation of axial velocity of droplets (includes all droplet sizes) and gas-phase are compared with experimental data as depicted in Fig. 11. An overall favorable agreement is found between DNS results and measurements. Similar statistics for the radial profiles of droplet averaged radial velocity and corresponding standard deviations obtained from DNS are compared to experimental measurements in Fig. 12, yielding good agreement. In Fig. 13, computed radial profiles of gas-phase mean excess temperature are compared with measurements for various stream-wise locations. The radial spread of the spray flame and temperature trends are well reproduced, with reasonable agreement between DNS results and measurements. However, discrepancies in the computed gas-phase temperature can be discerned, for example the overestimated temperature around the radial location $r/D = 1$, and the underestimated temperature close to the flame axis at the stream-wise location

$x/D = 10$. Such deviations are attributed to the limitations of the two-step simplified chemistry model [61] for Ethanol combustion reaction. However, in the experiment, gas-phase temperature was measured using thermocouples [45] which would have introduced errors in the measurements, in the form of lower gas-phase temperatures being measured than the real values. Such errors are associated with the cooling effect arising from droplet collisions with the thermocouples, and would be more severe at the stream-wise location of $x/D = 10$ which is relatively closer to the nozzle exit with high droplet counts.

6.2. Combustion noise results

Based on the quality of the DNS results for both flames, the acoustic source term $q_{e,rf}$ required for the computations of the acoustic fields generated by the flames is evaluated using the DNS solution. The source term $q_{e,rf}$ is examined in terms of its spatial distribution and strength for both the flames. The instantaneous distributions of the source term $q_{e,rf}$ are illustrated in Fig. 14 for the non-premixed flame H3 (left) and the spray flame EtF3 (right). In both the flames, the strongest acoustic sources are primarily located in the regions influenced by the unsteady heat release of combustion reaction. And this is evident in Fig. 14, where the strongest acoustic sources in both flames are situated within the red lines, which represent the iso-surfaces of stoichiometric mixture fraction Z_{st} of the respective flames ($Z_{st} = 0.3$ for H3 flame and $Z_{st} = 0.1$ for EtF3 flame). For the H3 flame, the strongest sources are located in the region $0 \leq x \leq 160$ mm and beyond $x \geq 200$ mm the source strength is quite diminished. With increasing distance from the nozzle exit, the amount of fuel available for combustion

decreases, therefore, the effect of one of the dominant source mechanisms of combustion noise in $q_{e,rf}$ i.e., the unsteady heat release rate also decreases with increasing downstream distance.

In case of the spray flame EtF3, the instantaneous distribution of source term $q_{e,rf}$ shows that the acoustic sources extend over a larger axial region compared to the H3 flame. This is due to the fact that, unlike the gaseous non-premixed H3 flame, the spray flame EtF3 has fuel injected in the form of liquid droplets and the unburned droplets that get convected further downstream, provide the fuel necessary for additional heat release process. Hence, strong acoustic sources corresponding to the dominant source mechanism in $q_{e,rf}$ can be seen even up to $x = 260$ mm. Furthermore, the source term $q_{e,rf}$ is stronger in case of the spray flame EtF3 compared to the non-premixed flame H3. Since the spray flame EtF3 has a piloted burner configuration at the inflow, the high temperature annular pilot flame that surrounds the central Ethanol/Air jet stream is a significant factor, that leads to stronger acoustic sources ($q_{e,rf}$) in the spray flame EtF3 compared to the non-premixed flame H3. Moreover, in Fig. 14 it can be seen that, in both the flames some acoustic sources are also present outside the iso-surfaces of stoichiometric mixture fraction Z_{st}. Contrary to the acoustic sources ($q_{e,rf}$) confined within the iso-surface of Z_{st} (for which one of the dominant source mechanisms is the unsteady heat release rate), the acoustic sources on the outside are produced by various other source mechanisms included in the source term $q_{e,rf}$, which results in the unsteady transport of the density field. This leads to some source contributions in the far downstream regions and outside the iso-surface of Z_{st}, even though heat release (chemical reaction) processes are not

necessarily occurring in those regions.

First, the combustion noise results obtained from the DNS/APE-RF approach are validated against experimental data for the turbulent non-premixed flame H3. The sound intensity level spectra of the H3 flame, computed from the CAA simulation are compared with measurements in Fig. 15. The positions in the far-field where these spectra have been computed, are the same positions at which the microphones were used to measure the sound intensity spectra in the experiment conducted by Piscoya et al. [96]. Each position at which the spectra are computed, corresponds to a different radiation angle θ with the flame axis. Some discrepancies in the computed sound intensities are attributed to the interpolation errors in the acoustic source term. This is because, the source term $q_{e,rf}$ which is computed on the DNS grid, has to be interpolated onto the CAA grid and the CAA mesh is not typically aligned with the DNS mesh at certain places within the overlapping source region, which might introduce errors in the CAA solution. However, the overall agreement between the computed and measured sound intensity spectra is mostly favourable at all positions for the H3 flame, in terms of the sound intensity levels, spectral content and shapes.

Based on this validation, the hybrid DNS/APE-RF approach is used to investigate the combustion generated acoustic field of the turbulent spray flame EtF3. Previous experimental investigations [19, 20, 97] have reported that open flame combustion noise has a unique and nearly universal spectral shape. Furthermore, it was also found that for open turbulent flames with round burner configurations, the spectral shape of combustion noise is not affected by parameters, such as flow velocity, turbulence intensity,

fuel consumption rate, flame temperature and type of fuel. Although the acoustic power, sound pressure levels and frequency at the spectral peak are significantly influenced by the above parameters. By performing extensive measurements of combustion noise in an earlier experimental study conducted by Tam et al. [98], it was demonstrated that the spectral shape of combustion noise is the same as the similarity spectrum of large turbulence structures noise of high-speed jets, as discovered by Tam, Golebiowski and Seiner [99]. This similarity spectrum can be constructed using an analytical spectral shape formula provided in [98, 99]. Moreover, the spectral shape of combustion noise, and the frequency and sound pressure level at the peak of the spectrum, exhibited nearly uniform directivity (remained unaltered with variation in the direction of noise radiation) [98].

Therefore, as depicted in Fig. 16, the sound pressure spectra of the open turbulent spray flame EtF3 computed from the CAA solution, are compared to the combustion noise similarity spectrum proposed by Tam et al. [98]. In Fig. 16, the combustion noise similarity spectrum is represented by the dotted curve and has been displaced vertically for comparison with the computed sound pressure spectra. The abscissa in these plots represent the normalized frequency, where f is the spectral frequency and f_p is the frequency corresponding to the peak of the spectrum, known as peak frequency. The computed sound pressure spectra of combustion noise emitted by the spray flame EtF3, are somewhat comparable to the combustion noise similarity spectrum proposed by Tam et al. [98]. However, the similarity spectrum does not completely capture all the features of the spray flame's combustion noise spectra. Specially the plateau of nearly constant sound pressure levels

(discussed later) in the range $3 < f/f_p \leq 8$. The combustion noise spectra of the spray flame EtF3 do not exhibit the monotone decrease in sound pressure level (for $f > f_p$), as shown by the similarity spectrum of Tam et al. [98]. But, the shapes of the computed combustion noise spectra are similar, regardless of the radiation angle θ. Moreover, the sound pressure levels at the spectral peaks are found to be nearly the same, irrespective of the radiation angle. In this sense, the combustion noise characteristics of the open turbulent spray flame EtF3 are similar to those of open turbulent non-premixed flames in general [24, 37].

In a previous experimental investigation on the combustion noise radiation from turbulent premixed flames conducted by Rajaram and Lieuwen [21], it was reported that the acoustic spectra have a power law dependence upon frequency of the form $f^{-\alpha}$ for $f > f_p$. Their measurements showed that the exponent α lies in the range $\alpha = 2.1 - 3.2$. Clavin and Siggia [31] also theoretically predicted such a power law dependence of the acoustic power spectrum of combustion noise emitted by turbulent premixed flames. They predicted the value of the exponent $\alpha = 2.5$, which means that the acoustic power rolls off with frequency as $f^{-2.5}$. In Fig. 17, the acoustic power spectra of the spray flame EtF3 computed from the CAA simulation, are shown for various positions. Fig. 17(a) shows the acoustic power spectra computed for the positions at a constant radial distance of $y = 400$ mm from the flame axis and at increasing stream-wise distances from the burner exit, while Fig. 17(b) shows the acoustic power spectra for positions at the same stream-wise locations as in Fig. 17(a), but at a fixed radial distance of $y = 480$ mm from the flame axis. It is observed that in the frequency range of 300 Hz $< f <$

1000 Hz, the acoustic power approximately rolls off according to the power law $f^{-2.4}$ (i.e. $\alpha = 2.4$) at all the positions. The present value of the exponent α is consistent with the measured range of α by Rajaram and Lieuwen [21]. The fact that the combustion noise spectra of the spray flame EtF3, decay with frequency according to this power law (in the frequency range 300 Hz $< f <$ 1000 Hz), is likely due to the partially-premixed nature of the spray flame.

Next, the sound pressure spectra computed for the far-field positions at increasing stream-wise distances from the nozzle exit, but at a constant radial distance of $y = 400$ mm and $y = 480$ mm from the flame axis are depicted in Figs. 18(a) and 18(b), respectively. Note that each position in Fig. 18 corresponds to a different radiation angle θ to the flame axis. The CAA computed noise spectra of the spray flame are broadband. Considering Fig. 18(a), it is observed that the sound pressure levels and spectral shapes (for the positions at a fixed radial distance from the flame axis and different stream-wise locations) are virtually similar at all radiation angles for the low-frequencies (i.e. for $f <$ 1000 Hz).

For the positions corresponding to radiation angles greater than 43° in Fig. 18(a), i.e., $(x, y; \theta)$ = (0, 400 mm; 90°), (48 mm, 400 mm; 83°), (144 mm, 400 mm; 70°), (240 mm, 400 mm; 60°) and (336 mm, 400 mm; 50°), it is found that the spectral shapes and sound pressure levels are quite similar for the entire frequency range presented. The reason for this is attributed to the extended distribution of the acoustic sources of the spray flame EtF3, in the axial direction as depicted in Fig. 14. Hence, a cone of silence (region in the acoustic field subjected to diminished noise irradiation, which is discussed

later) where the sound pressure levels of the high-frequency noise emissions undergo attenuation, is not observed for the positions corresponding to radiation angles greater than 43°.

Furthermore, for the same positions (corresponding to radiation angles greater than 43°) in Fig. 18(a) mentioned above, the sound pressure levels are nearly constant in the frequency range of 1000 Hz < f < 3000 Hz, forming a plateau in the frequency spectra, which is qualitatively represented by the red dash-dotted horizontal line. This characteristic is very similar to that observed in a previous experimental study, for noise emissions from turbulent non-premixed flames by Singh et al. [24], where a plateau of constant sound pressure level was observed in the noise spectra of DLR-A and DLR-B flames [43] in the frequency range 400 Hz < f < 2000 Hz. In the present study, the existence of such a plateau of nearly constant sound pressure level in the frequency range 1000 Hz < f < 3000 Hz, could be attributed to the strong acoustic sources existing up to farther downstream locations in the EtF3 spray flame (see Fig. 14). Moreover, for f > 3000 Hz the sound pressure level decreases in an almost linear fashion for all the positions, and this characteristic is also similar to that of the sound pressure spectra of turbulent non-premixed flames [24]. However, in Fig. 18(a) it is found that, for the high-frequency noise emissions (f > 1000 Hz), suppression of sound pressure levels with increasing downstream location from the nozzle exit (which corresponds to decreasing radiation angle to the flame axis), is apparent for the positions $(x, y; \theta)$ = (528 mm, 400 mm; 37°) and (624 mm, 400 mm; 33°). For the position $(x, y; \theta)$ = (432 mm, 400 mm; 43°), such reduction in sound pressure levels becomes appreciable for f > 4000 Hz. The reduction

in sound pressures of the high-frequency noise emissions is more pronounced for the downstream positions corresponding to $\theta < 43°$, which would create a relative cone of silence at these far downstream positions (at low radiation angles to the flame axis).

Similar characteristics are observed in the computed sound pressure spectra for the positions in Fig. 18(b). Such as, the similar spectral shapes and sound pressure levels for the low-frequencies (f $<$ 1000 Hz); the plateau of virtually constant sound pressure level in the frequency range 1000 Hz $<$ f $<$ 2600 Hz, for the positions corresponding to radiation angles greater than 42°, followed by an almost linear decrease of the sound pressure level for f $>$ 2600 Hz; similar spectral shapes and sound pressure levels for the entire frequency range presented (for positions corresponding to $\theta > 42°$); and the reduction in sound pressure levels of the high-frequency noise emissions (f $>$ 1000 Hz) at the far downstream positions (corresponding to low radiation angles to the flame axis, $\theta \leq 42°$) of $(x, y; \theta)$ = (528 mm, 480 mm; 42°) and (624 mm, 480 mm; 38°).

This downstream attenuation of high-frequency noise emissions is caused by refraction effects due to temperature non-uniformities within the flame [100], and such weak directivity in the high-frequency noise emissions has been confirmed in previous investigations of turbulent non-premixed flames [24, 33]. Furthermore, the APE-RF system solved in the CAA simulation is capable of capturing such acoustic refraction effects of the high-frequency noise components, produced by gradients in mean sound speed within the turbulent flame [101]. The temperature non-uniformities existing in the flame lead to gradients in the speed of sound, which is illustrated by the distribu-

tion of mean speed of sound in the turbulent spray flame EtF3 in Fig. 19. When the high-frequency acoustic waves propagate in the flame downstream direction, they get refracted away from the flame axis upon interacting with the mean sound speed gradients within the flame. Such acoustic refractions due to temperature dependent variations in the mean speed of sound, are mostly relevant in the flame downstream direction [102]. Furthermore, it is evident from Figs. 18(a) and 18(b) that the refraction effect (at the far downstream positions) becomes stronger with increasing frequency, i.e. the higher the noise emission frequency, the stronger the attenuation of its sound pressure level.

To analyse the variations in noise spectra with varying radial location from the flame axis, the sound pressure spectra of the spray flame EtF3 computed at various positions are shown in Fig. 20. Each of the plots in Figs. 20(a) - 20(e) show the sound pressure spectra computed for positions at a fixed stream-wise location (x) from the burner exit, and at different radial locations (y) from the flame axis. Some general tendencies are observed in these plots. Such as, the spectral shapes being qualitatively similar for all positions, and the decrease in sound pressure level with increasing radial distance (at a fixed stream-wise location) from the flame axis for most frequencies. However, the reduction in sound pressure level with increasing radial distance from the flame axis, is more appreciable for the noise emissions at higher frequencies (f $>$ 1000 Hz). But, the extent of this reduction in sound pressure level of the high-frequency (f $>$ 1000 Hz) noise emissions (with increasing radial distance from the flame axis), is different for the noise spectra depending upon the stream-wise location [Figs. 20(a)

- 20(e)], because the acoustic refraction effects discussed previously play an important role. Also, for the positions whose radial locations are quite far away from the flame axis, i.e. $y \geq 480$ mm, it is observed that the width of the sound pressure level plateau in the noise spectra is reduced slightly from the high-frequency side (plateau lies in the frequency range 1000 Hz $<$ f $<$ 2600 Hz).

Lastly, the frequency-specific noise directivity effects of the spray flame EtF3 are detailed in Fig. 21. For this exercise, the sound pressure levels corresponding to several different frequencies have been computed from the CAA solution, at various positions that lie on a circular arc of radius $R = 525$ mm in the central x-y plane of the CAA grid, and centered at the nozzle exit i.e. at $(x,y,z) = (0,0,0)$. Each position on the circular arc is at an angle to the flame axis ranging from 20° to 90°. The sound pressure levels at the low-frequencies (f $<$ 1000 Hz) in Figs. 21(a) and 21(b), are nearly the same for all radiation angles indicating a monopole behavior. This monopole character at the low-frequencies is attributed to the unsteady heat release rate, which also happens to be one of the dominant source mechanisms of combustion noise in the source term $q_{e,rf}$. Moreover, the sound pressure levels of the low-frequency noise emissions are greater than those of the higher frequency noise emissions (f $>$ 1000 Hz). In the higher frequency range, the sound pressure levels tend to decrease with increasing frequency as shown in Figs. 21(c) - 21(l). Hence, most of the acoustic energy of combustion noise generated by the spray flame EtF3 is situated within the low-frequencies, which confirms its low-frequency characteristic, similar to that of low Mach number premixed [16, 72] and non-premixed flames [24, 33]. The noise directivity

starts deviating from the monopole behavior in Fig. 21(c) for f = 1181.81 Hz. At further higher frequencies, such as in Figs. 21(d) - 21(l), the directivity of noise emissions starts exhibiting multipole-type character. This non-isotropic behavior of the high-frequency noise emissions is attributed to the source mechanisms other than the unsteady heat release in the source term $q_{e,rf}$, which contribute to the sound pressures at high-frequencies. Since, the high-frequency noise emissions are more susceptible to acoustic refraction effects (caused by mean sound speed gradients within the flame) than the low-frequency noise emissions, departure from monopole/isotropic behavior of the noise directivity at high-frequencies is thus evident. Therefore, the higher the noise emission frequency, the stronger the directivity of sound pressure level (stronger deviation from isotropic character of sound pressure level).

7. Conclusions

The relatively new numerical framework of the hybrid CFD/CAA approach was applied to the turbulent spray flame EtF3 (Re = 19700, fuel = Ethanol), to predict and analyze the radiation of combustion generated noise. In this two-step framework, the first step involves a DNS of the reacting flow-field of the turbulent flame (within which the sources exciting acoustic waves are present), while the second step involves a CAA simulation that is performed by solving the Acoustic Perturbation Equations extended for Reacting Flows (APE-RF), to capture the acoustic wave propagation all the way into the far-field. In order to incorporate the additional effect of density variations caused by fuel droplet evaporation, the source term ($q_{e,rf}$) domi-

nating the excitation of acoustic waves in combustion noise, was reformulated for the spray flame EtF3. First, the hybrid approach was used to simulate the benchmark experimental open turbulent non-premixed Hydrogen flame H3 ($Re = 10000$). The results obtained from the hybrid DNS/APE-RF approach for the non-premixed Hydrogen flame's flow-field statistical quantities, as well as radiated sound intensities were extensively validated against experimental data, to assess the fidelity of the numerical procedures employed in the hybrid DNS/APE-RF approach. Next, the hybrid DNS/APE-RF approach was applied to the experimental open turbulent spray flame EtF3, to simulate its two-phase reacting flow-field and combustion generated acoustic field, with the objective of predicting and analyzing the noise radiation behavior.

The results obtained from the hybrid DNS/APE-RF approach for combustion noise spectra of the spray flame EtF3 in the far-field, revealed characteristics similar to those of turbulent premixed and non-premixed flames in general, such as, the broadband shape of the sound pressure spectra; the power law dependence of the acoustic power spectra of the form $f^{-2.4}$, in the frequency range 300 Hz $<$ f $<$ 1000 Hz; virtually same spectral content in the low-frequencies (f $<$ 1000 Hz) and a nearly constant sound pressure level plateau for frequencies greater than 1000 Hz and up to 3000 Hz, for the positions at a fixed radial distance from the flame axis and at various stream-wise locations from the burner exit (corresponding to different radiation angles to the flame axis); and attenuation of the high-frequency noise radiated towards the far downstream positions (at low radiation angles to the flame axis), which was caused by acoustic refraction effects stemming from the sound speed gradients (which is in turn caused by the temperature

non-uniformities) within the flame. Furthermore, combustion noise generated by the spray flame exhibited low-frequency characteristic, implying that most of the acoustic energy was situated within the low-frequencies, similar to turbulent premixed and non-premixed flames. Therefore, the hybrid DNS/APE-RF approach used in this study is capable of accurately capturing the characteristics of radiation of combustion generated noise, of the spray flame up to the far-field.

Acknowledgements

This research was partially supported by MEXT (Ministry of Education, Culture, Sports, Science and Technology – Japan) as "Priority issue on Post-K computer" (Accelerated Development of Innovative Clean Energy Systems), and by MEXT Grant in Aid (No.16H04278).

References

[1] J. E. Ffowcs Williams, Hydrodynamic noise, Annu. Rev. Fluid Mech. 1 (1969) 197–222.

[2] J. E. Ffowcs Williams, Aeroacoustics, Annu. Rev. Fluid Mech. 9 (1977) 447–468.

[3] M. E. Goldstein, Aeroacoustics of turbulent shear flows, Annu. Rev. Fluid Mech. 16 (1984) 263–285.

[4] C. K. W. Tam, Supersonic jet noise, Annu. Rev. Fluid Mech. 27 (1995) 17–43.

[5] A. P. Dowling, S. R. Stow, Acoustic analysis of gas turbine combustors, J. Propul. Power 19 (2003) 751–764.

[6] Y. Liu, A. P. Dowling, N. Swaminathan, R. Morvant, M. A. Macquisten, L. F. Caracciolo, Prediction of combustion noise for an aeroengine combustor, J. Propul. Power 30 (2013) 114–122.

[7] S. Candel, Combustion dynamics and control: Progress and challenges, Proc. Combust. Inst. 29 (2002) 1–28.

[8] S. Candel, D. Durox, S. Ducruix, A. L. Birbaud, N. Noiray, T. Schuller, Flame dynamics and combustion noise: Progress and challenges, Int. J. Aeroacoust. 8 (2009) 1–56.

[9] S. Tachibana, K. Saito, T. Yamamoto, M. Makida, T. Kitano, R. Kurose, Experimental and numerical investigation of thermoacoustic instability in a liquid-fuel aero-engine combustor at elevated pressure: Validity of large-eddy simulation of spray combustion, Combust. Flame 162 (6) (2015) 2621–2637.

[10] T. Lieuwen, V. Yang, Combustion instabilities in gas turbine engines: Operational experience, fundamental mechanisms, and modeling, Prog. Astronaut. Aeronaut. 210.

[11] W. C. Strahle, Combustion noise, Prog. Energy Combust. Sci. 4 (1978) 157–176.

[12] J. E. Ffowcs Williams, M. S. Howe, The generation of sound by density inhomogeneities in low mach number nozzle flows, J. Fluid Mech. 70 (1975) 605–622.

[13] F. E. Marble, S. Candel, Acoustic disturbance from gas non-uniformities convected through a nozzle, J. Sound Vib. 55 (1977) 225–243.

[14] M. S. Howe, Indirect combustion noise, J. Fluid Mech. 659 (2010) 267–288.

[15] A. P. Dowling, Y. Mahmoudi, Combustion noise, Proc. Combust. Inst. 35 (2015) 65–100.

[16] T. J. B. Smith, J. K. Kilham, Noise generation by open turbulent flames, J. Acoust. Soc. Am. 35 (1963) 715–724.

[17] R. B. Price, I. R. Hurle, T. M. Sugden, Optical studies of the generation of noise in turbulent flames, Proc. Combust. Inst. 12 (1968) 1093–1101.

[18] W. C. Strahle, B. N. Shivashankara, A rational correlation of combustion noise results from open turbulent premixed flames, Proc. Combust. Inst. 15 (1975) 1379–1385.

[19] S. Kotake, K. Takamoto, Combustion noise: Effects of the shape and size of burner nozzle, J. Sound Vib. 112 (1987) 345–354.

[20] S. Kotake, K. Takamoto, Combustion noise: Effects of velocity turbulence of unburned mixture, J. Sound Vib. 139 (1990) 9–20.

[21] R. Rajaram, T. Lieuwen, Acoustic radiation from turbulent premixed flames, J. Fluid Mech. 637 (2009) 357–385.

[22] N. Ohiwa, K. Tanaka, S. Yamaguchi, Noise characteristics of turbulent diffusion flames with coherent structure, Combust. Sci. Tech. 90 (1993) 61–78.

[23] S. A. Klein, J. B. W. Kok, Sound generation by turbulent non-premixed flames, Combust. Sci. Tech. 149 (1999) 267–295.

[24] K. K. Singh, S. H. Frankel, J. P. Gore, Study of spectral noise emissions from standard turbulent nonpremixed flames, AIAA Journal 42 (2004) 931–936.

[25] C. Hirsch, J. Wäsle, A. Winkler, T. Sattelmayer, A spectral model for the sound pressure from turbulent premixed combustion, Proc. Combust. Inst. 31 (2007) 1435–1441.

[26] Y. Liu, T. Echekki, Modelling of combustion noise spectrum using temporal correlations of heat release rate from turbulent premixed flames, AIAA paper 2015-2970 (2015).

[27] A. Haghiri, M. Talei, M. J. Brear, E. R. Hawkes, Sound generation by turbulent premixed flames, J. Fluid Mech. 843 (2018) 29–52.

[28] S. Schlimpert, A. Feldhusen, J. H. Grimmen, B. Roidl, M. Meinke, W. Schröder, Hydrodynamic instability and shear layer effects in turbulent premixed combustion, Combust. Flame 162 (2015) 345–367.

[29] S. Schlimpert, S. Hemchandra, M. Meinke, W. Schröder, Hydrodynamic instability and shear layer effect on the response of an acoustically excited laminar premixed flame, Combust. Flame 162 (2015) 345–367.

[30] S. Schlimpert, M. Meinke, W. Schröder, Nonlinear analysis of an acoustically excited laminar premixed flame, Combust. Flame 163 (2016) 337–357.

[31] P. Clavin, E. D. Siggia, Turbulent premixed flames and sound generation, Combust. Sci. Tech. 78 (1991) 147–155.

[32] M. Ihme, H. Pitsch, D. Bodony, Radiation of noise in turbulent non-premixed flames, Proc. Combust. Inst. 32 (2009) 1545–1553.

[33] M. Ihme, H. Pitsch, On the generation of direct combustion noise in turbulent non-premixed flames, Int. J. Aeroacoust. 11 (2012) 25–78.

[34] F. Flemming, A. Nauert, A. Sadiki, J. Janicka, H. Brick, R. Piscoya, M. Ochmann, P. Költzsch, A Hybrid Approach for the evaluation of the radiated noise from a turbulent non-premixed jet flame based on large eddy simulation and equivalent source and boundary element methods, 12^{th} International Congress on Sound and Vibration ICSV12, Lisbon, Portugal, 2005.

[35] F. Flemming, A. Sadiki, J. Janicka, Investigation of combustion noise using a LES/CAA hybrid approach, Proc. Combust. Inst. 31 (2007) 3189–3196.

[36] B. Mühlbauer, R. Ewert, O. Kornow, B. Noll, Evaluation of the RPM approach for the simulation of broadband combustion noise, AIAA Journal 48 (7) (2010) 1379–1390.

[37] B. Mühlbauer, R. Ewert, O. Kornow, B. Noll, Broadband combustion

noise simulation of open non-premixed turbulent jet flames, Int. J. Aeroacoust. 11 (1) (2012) 1–24.

[38] T. P. Bui, W. Schröder, M. Meinke, Numerical analysis of the acoustic field of reacting flows via acoustic perturbation equations, Comput. Fluids 37 (2008) 1157–1169.

[39] T. P. Bui, M. Ihme, W. Schröder, H. Pitsch, Analysis of different sound source formulations to simulate combustion generated noise using a hybrid LES/APE-RF method, Int. J. Aeroacoustics 8 (2009) 95–124.

[40] R. Ewert, W. Schröder, Acoustic perturbation equations based on flow decomposition via source filtering, J. Comput. Physics 188 (2003) 365–398.

[41] S. Schlimpert, S. R. Koh, K. Pausch, M. Meinke, W. Schröder, Analysis of combustion noise of a turbulent premixed slot jet flame, Combust. Flame 175 (2017) 292–306.

[42] K. Pausch, S. Herff, S. Schlimpert, M. Meinke, W. Schröder, Acoustic flame response of a round and a slot burner, AIAA paper 2017-3360 (2017).

[43] R. Barlow, (Ed.), Proceedings of the TNF workshops, Sandia National Laboratories, Livermore, CA, 1996-2004, available at www.ca.sandia.gov/TNF.

[44] D. G. Pfuderer, A. A. Neuber, G. Früchtel, E. P. Hassel, J. Janicka, Turbulence modulation in jet diffusion flames: Modeling and experiments, Combust. Flame 106 (1996) 301–317.

[45] J. D. Gounder, A. Kourmatzis, A. R. Masri, Turbulent piloted dilute spray flames: Flow fields and droplet dynamics, Combust. Flame 159 (2012) 3372–3397.

[46] W. L. Grosshandler, RADCAL: A narrow-band model for radiation calculations in a combustion environment, NIST Technical Note 1402 (1993).

[47] R. S. Barlow, A. N. Karpetis, J. H. Frank, J.-Y. Chen, Scalar profiles and NO formation in laminar opposed-flow partially premixed methane/air flames, Combust. Flame 127 (2001) 2102–2118.

[48] A. L. Pillai, R. Kurose, Numerical investigation of combustion noise in an open turbulent spray flame, Applied Acoustics 133 (2018) 16–27.

[49] C. T. Crowe, M. P. Sharma, D. E. Stock, The Particle-Source-In Cell (PSI-CELL) model for gas-droplet flows, J. Fluids Eng. 99 (1977) 325–332.

[50] J. Bellan, K. Harstad, Analysis of the convective evaporation of nondilute clusters of drops, Int. J. Heat Mass Transfer 30 (1) (1987) 125–136.

[51] R. S. Miller, K. Harstad, J. Bellan, Evaluation of equilibrium and nonequilibrium evaporation models for many-droplet gas-liquid flow simulations, Int. J. Multiphase Flow 24 (6) (1998) 1025–1055.

[52] R. S. Miller, J. Bellan, Direct numerical simulation of a confined three-dimensional gas mixing layer with one evaporating hydrocarbon-droplet laden stream, J. Fluid Mech. 384 (1999) 293–338.

[53] T. Kitano, K. Kaneko, R. Kurose, S. Komori, Large-eddy simulations of gas– and liquid–fueled combustion instabilities in back-step flows, Combust. Flame 170 (2016) 63–78.

[54] J. Bellan, M. Summerfield, Theoretical examination of assumptions commonly used for the gas phase surrounding a burning droplet, Combust. Flame 33 (1978) 107–122.

[55] M. Nakamura, F. Akamatsu, R. Kurose, M. Katsuki, Combustion mechanism of liquid fuel spray in a gaseous flame, Phys. Fluids 17 (12) (2005) 123301.

[56] R. Kurose, H. Makino, S. Komori, M. Nakamura, F. Akamatsu, M. Katsuki, Effects of outflow from the surface of a sphere on drag, shear lift, and scalar diffusion, Phys. Fluids 15 (8) (2003) 2338–2351.

[57] H. Watanabe, R. Kurose, S.-M. Hwang, F. Akamatsu, Characteristics of flamelets in spray flames formed in a laminar counterflow, Combust. Flame 148 (4) (2007) 234–248.

[58] M. Talei, M. J. Brear, E. R. Hawkes, A parametric study of sound generation by premixed laminar flame annihilation, Combust. Flame 159 (2) (2012) 757–769.

[59] M. Talei, M. J. Brear, E. R. Hawkes, A comparative study of sound generation by laminar, combusting and non-combusting jet flows, Theor. Comput. Fluid Dyn. 28 (2014) 385–408.

[60] N. M. Marinov, C. K. Westbrook, W. J. Pitz, Detailed and global

chemical kinetics model for hydrogen, Transport Phenomena in Combustion, edited by S. H. Chen, Vol. 1, Taylor and Francis, Washington, D.C., 1996, pp. 118–129.

[61] C. K. Westbrook, F. L. Dryer, Simplified reaction mechanisms for the oxidation of hydrocarbon fuels in flames, Combust. Sci. Tech. 27 (1981) 31–43.

[62] A. P. Wandel, N. Chakraborty, E. Mastorakos, Direct numerical simulations of turbulent flame expansion in fine sprays, Proc. Combust. Inst. 32 (2009) 2283–2290.

[63] S. P. Malkeson, N. Chakraborty, Statistical analysis of scalar dissipation rate transport in turbulent partially premixed flames: A Direct Numerical Simulation study, Flow Turbul. Combust. 86 (1) (2011) 1–44.

[64] T. P. Dunstan, N. Swaminathan, K. N. C. Bray, R. S. Cant, Geometrical properties and turbulent flame speed measurements in stationary premixed V-flames using Direct Numerical Simulation, Flow Turbul. Combust. 87 (2–3) (2011) 237–259.

[65] T. P. Dunstan, N. Swaminathan, K. N. C. Bray, Influence of flame geometry on turbulent premixed flame propagation: A DNS investigation, J. Fluid Mech. 709 (2012) 191–222.

[66] D. H. Wacks, N. Chakraborty, E. Mastorakos, Statistical analysis of turbulent flame-droplet interaction: A direct numerical simulation study, Flow Turbul. Combust. 96 (2016) 573–607.

[67] D. H. Wacks, N. Chakraborty, Flame structure and propagation in turbulent flame-droplet interaction: A Direct Numerical Simulation analysis, Flow Turbul. Combust. 96 (2016) 1053–1081.

[68] R. Ewert, W. Schröder, On the simulation of trailling edge noise with a hybrid LES/APE method, J. Sound Vib. 270 (2004) 509–524.

[69] D. G. Crighton, A. P. Dowling, J. E. Ffowcs Williams, M. Heckl, F. G. Leppington, Modern Methods in Analytical Acoustics, Springer, 1992.

[70] T. P. Bui, W. Schröder, M. Meinke, Acoustic perturbation equations for reacting flows to compute combustion noise, Int. J. Aeroacoustics 6 (2007) 335–355.

[71] W. Schröder, R. Ewert, Some concepts of LES-CAA coupling, LES for Acoustics, Cambridge University Press, 2005.

[72] B. N. Shivashankara, W. C. Strahle, J. C. Handley, Combustion noise radiation by open turbulent flames, AIAA paper 1973-1025 (1973).

[73] F. A. Williams, Combustion Theory, The Fundamental Theory of Chemically Reacting Flow Systems, Addison-Wesley, 1964.

[74] T. P. Bui, W. Schröder, Theoretical and Numerical Analysis of Broadband Combustion Noise, Springer Berlin Heidelberg, Berlin, Heidelberg, 2009, pp. 175–215.

[75] K. Luo, O. Desjardins, H. Pitsch, DNS of droplet evaporation and combustion in a swirling combustor, in: Annual Research Briefs, Center for Turbulence Research, NASA Ames/Stanford University, 2008.

[76] K. Luo, H. Pitsch, M. G. Pai, O. Desjardins, Direct numerical simulations and analysis of three-dimensional n-heptane spray flames in a model swirl combustor, Proc. Combust. Inst. 33 (2011) 2143–2152.

[77] S. B. Pope, Turbulent flows, UK: Cambridge University Press, 2000.

[78] K. Luo, T. Jin, S. Lu, J. Fan, DNS analysis of a three-dimensional supersonic turbulent lifted jet flame, Fuel 108 (2013) 691–698.

[79] T. Kitano, J. Nishio, R. Kurose, S. Komori, Evaporation and combustion of multicomponent fuel droplets, Fuel 136 (2014) 219–225.

[80] T. Kitano, T. Tsuji, R. Kurose, S. Komori, Effect of pressure oscillations on flashback characteristics in a turbulent channel flow, Energy Fuels 29 (10) (2015) 6815–6822.

[81] Y. Hu, R. Kurose, Nonpremixed and premixed flamelets LES of partially premixed spray flames using a two-phase transport equation of progress variable, Combust. Flame 188 (2018) 227–242.

[82] Y. Haruki, A. L. Pillai, T. Kitano, R. Kurose, Numerical investigation of flame propagation in fuel droplet arrays, Atomization and Sprays 28 (4) (2018) 357–388.

[83] V. Moureau, C. Bérat, H. Pitsch, An efficient semi-implicit compressible solver for large-eddy simulations, J. Comput. Physics 226 (2) (2007) 1256–1270.

[84] G.-S. Jiang, C.-W. Shu, Efficient implementation of weighted ENO schemes, J. Comput. Physics 126 (1996) 202–228.

[85] R. J. Kee, D.-L. Graham, J. Warnatz, M. E. Coltrin, J. A. Miller, A fortran computer code package for the evaluation of gas-phase, multicomponent transport properties, SANDIA Report No. SAND86-8246, Sandia National Laboratories, Albuquerque NM, Livermore CA (1986).

[86] R. J. Kee, F. M. Rupley, J. A. Miller, Chemkin-II: A FORTRAN chemical kinetics package for the analysis of gas-phase chemical kinetics, SANDIA Report No. SAND89-8009B, Sandia National Laboratories, Albuquerque NM, Livermore CA (1989).

[87] M. Klein, A. Sadiki, J. Janicka, A digital filter based generation of inflow data for spatially developing direct numerical or large eddy simulations, J. Comput. Physics 186 (2003) 652–665.

[88] A. M. Kempf, S. Wysocki, M. Pettit, An efficient, parallel low-storage implementation of Kleins turbulence generator for LES and DNS, Comput. Fluids 60 (2012) 58–60.

[89] C. Bogey, C. Bailly, Three-dimensional non-reflective boundary conditions for acoustic simulations: Far field formulation and validation test cases, Acta. Acust. united Ac. 88 (2002) 463–471.

[90] C. A. Kennedy, M. H. Carpenter, Several new numerical methods for compressible shear-layer simulations, Appl. Numer. Math. 14 (1994) 397–433.

[91] C. K. W. Tam, J. C. Webb, Dispersion-Relation-Preserving finite difference schemes for computational acoustics, J. Comput. Physics 107 (1993) 262–281.

[92] C. Bogey, C. Bailly, A family of low dispersive and low dissipative explicit schemes for flow and noise computations, J. Comput. Physics 194 (2004) 194–214.

[93] C. K. W. Tam, H. Shen, Direct computation of nonlinear acoustic pulses using high order finite difference schemes, AIAA Paper 93-4325 (1993).

[94] C. K. W. Tam, Computational aeroacoustics: Issues and methods, AIAA Journal 33 (10) (1995) 1788–1796.

[95] G. L. Brown, A. Roshko, On density effects and large structure in turbulent mixing layers, J. Fluid Mech. 64 (1974) 775–816.

[96] R. Piscoya, H. Brick, M. Ochmann, P. Költzsch, Equivalent source method and boundary element method for calculating combustion noise, Acta Acust. united Ac. 94 (4) (2008) 514–527.

[97] R. Rajaram, T. Lieuwen, Effect of approach flow turbulence characteristics on sound generation from premixed flames, AIAA Paper 2004-0461 (2004).

[98] C. K. W. Tam, N. N. Pastouchenko, J. Mendoza, D. Brown, Combustion noise of auxiliary power units, AIAA paper 2005-2829 (2005).

[99] C. K. W. Tam, M. Golebiowski, J. M. Seiner, On the two components of turbulent mixing noise from supersonic jets, AIAA paper 96-1716 (1996).

[100] W. C. Strahle, Some results in combustion generated noise, J. Sound Vib. 23 (1972) 113–125.

[101] T. P. Bui, W. Schröder, Acoustic wave refraction in open turbulent flames, Acta. Acust. united Ac. 95 (2009) 440–447.

[102] M. Ihme, M. Kaltenbacher, H. Pitsch, Numerical simulation of flow- and combustion-induced sound using a hybrid LES/CAA approach, Proceedings of the Summer Program, Center for Turbulence Research, 2006, pp. 497–510.

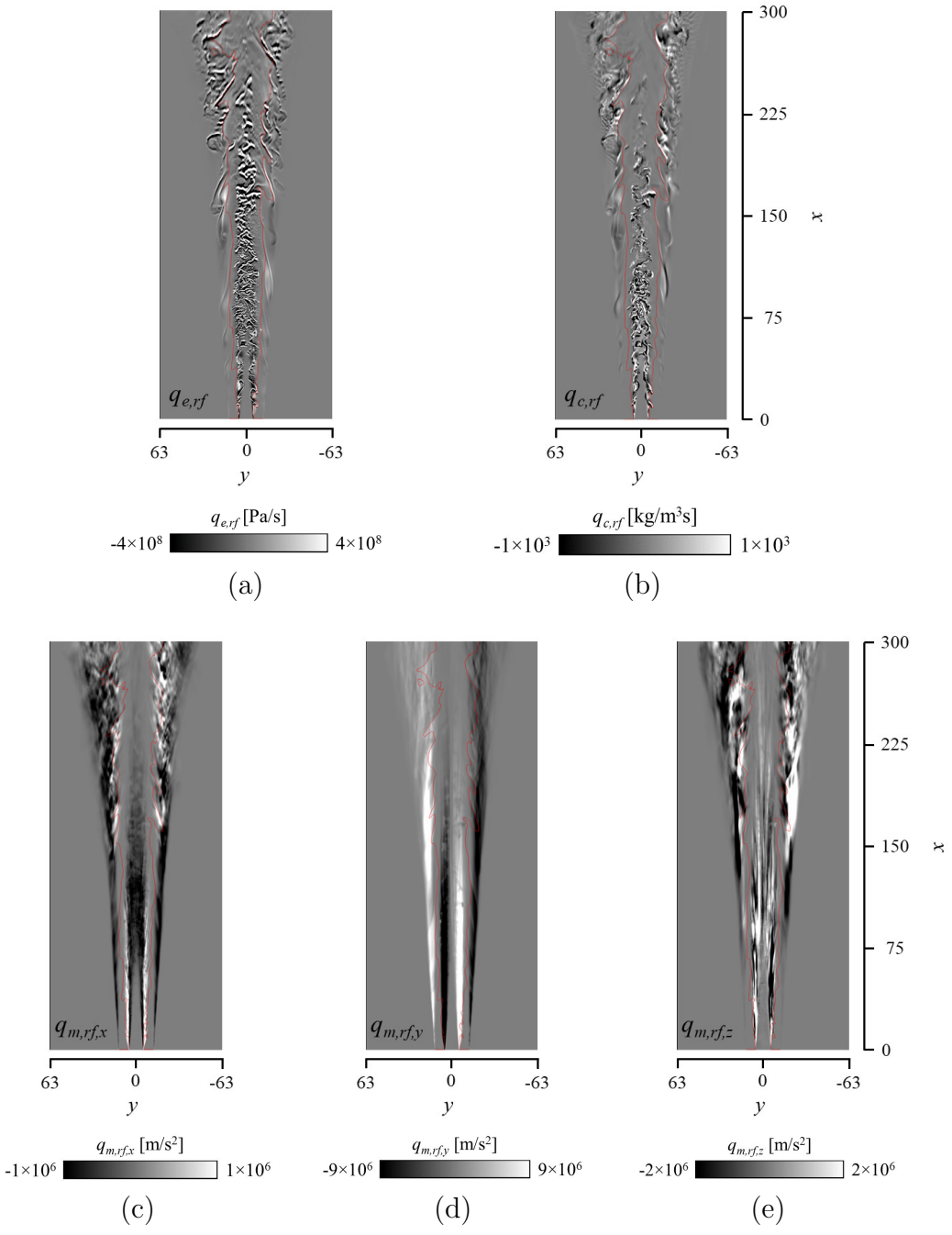

Figure 1: Instantaneous distributions of the acoustic source terms $q_{c,rf}$, $\boldsymbol{q}_{m,rf}$ and $q_{e,rf}$ given by Eqs. (38), (39) and (42), respectively for the turbulent piloted spray flame EtF3. (c), (d) and (e) represent the x-, y- and z- components, respectively, of the source term $\boldsymbol{q}_{m,rf}$. The red lines in each of the instantaneous source fields represent the iso-surfaces of stoichiometric mixture fraction ($Z_{st} = 0.1$) of the spray flame. Dimensions shown in the axial (x) and radial (y) directions are in mm.

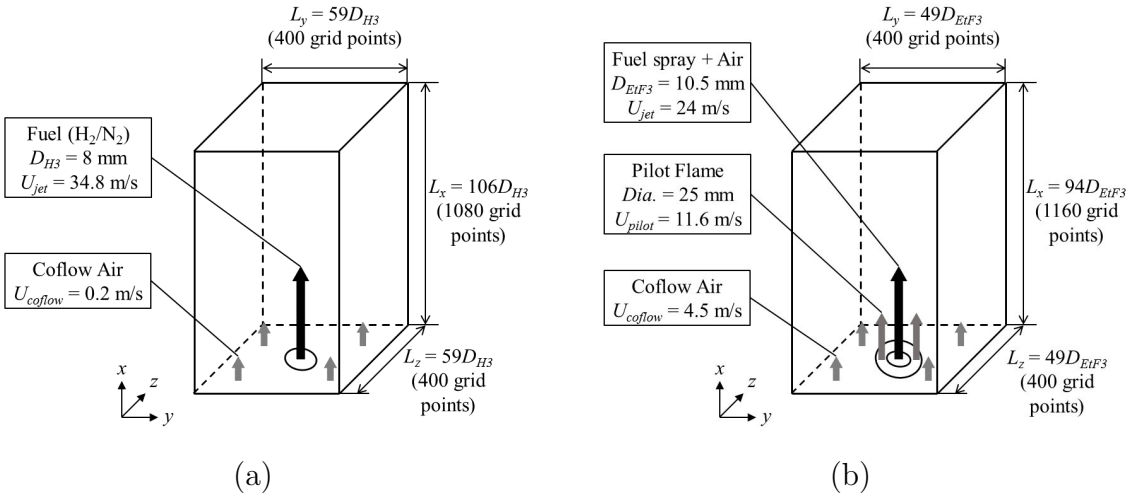

Figure 2: Schematics of the computational domains used for the DNS of (a) turbulent non-premixed Hydrogen flame H3 and (b) turbulent Ethanol spray flame EtF3.

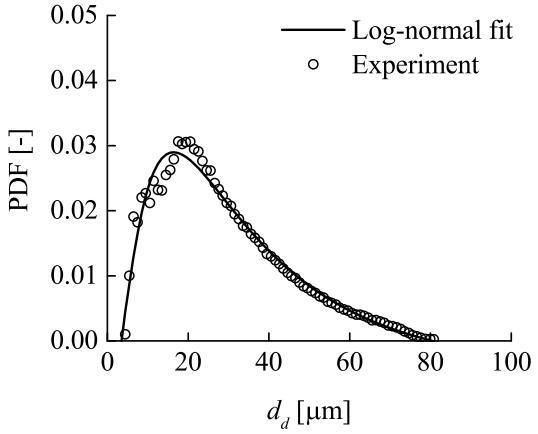

Figure 3: Droplet size distribution PDF of injected fuel droplets at the central jet nozzle inflow in the DNS (symbols represent experimental data [45]).

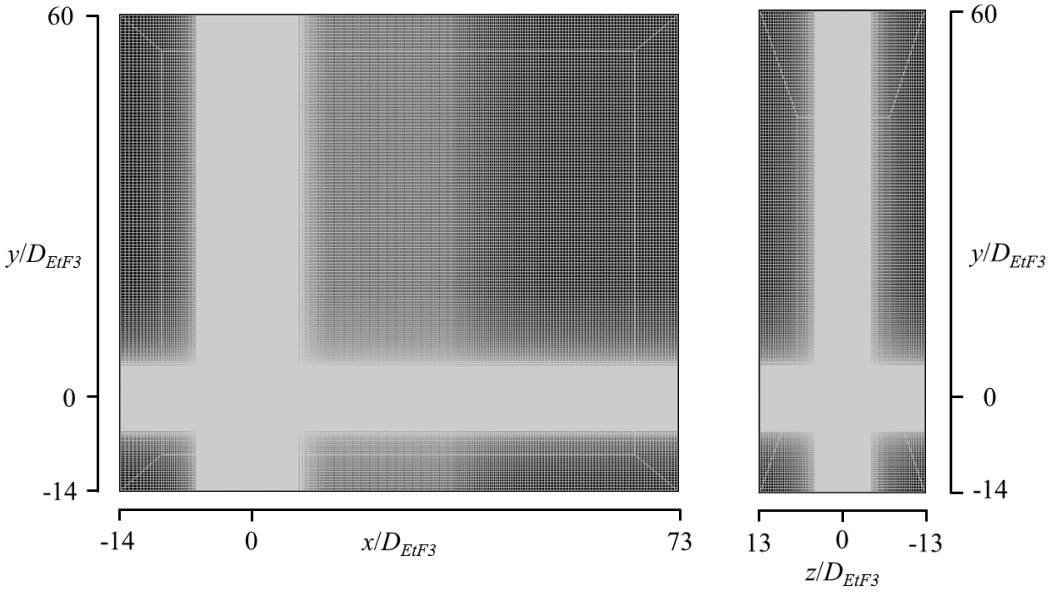

Figure 4: Cell distributions in the x-y and y-z planes of the Cartesian grid used in the CAA simulation of the spray flame EtF3 ($D_{EtF3} = 10.5$ mm).

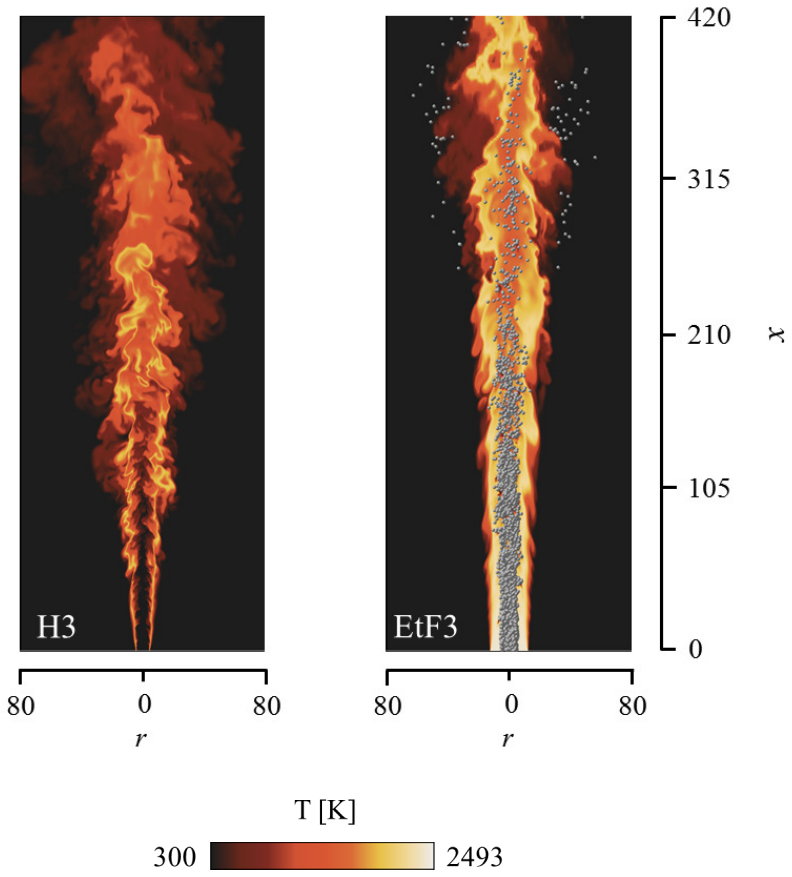

Figure 5: Instantaneous snapshots of the DNS computed temperature fields of the turbulent non-premixed flame H3 (left) and spray flame EtF3 (right). Lengths shown in the axial (x) and radial (r) directions are the same for both flames, with all dimensions being in mm. (Note: The actual DNS domain height in the axial direction is larger than the displayed height).

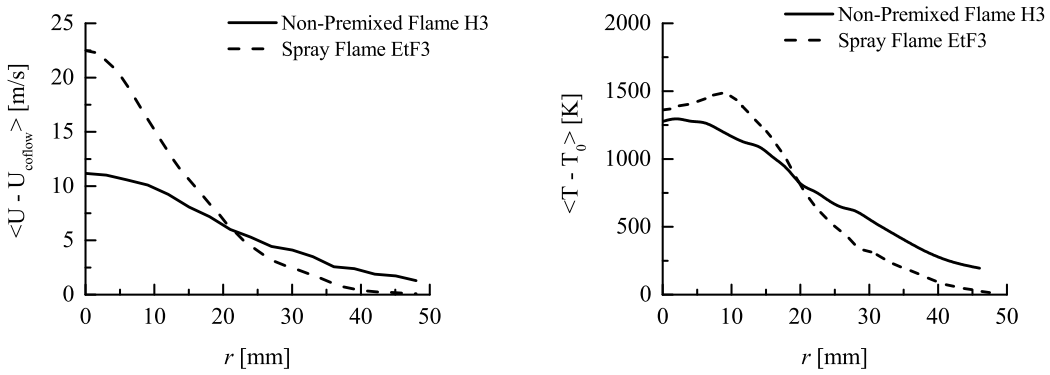

Figure 6: Radial profiles of mean axial velocity (left) and mean temperature (right) obtained from DNS for both the non-premixed flame H3 and the spray flame EtF3, at the stream-wise location of $x = 320$ mm from the burner exit of each flame. Here U_{coflow} is the coflow velocity and T_0 is the ambient temperature as listed in Tables 1 and 2 for the respective flames.

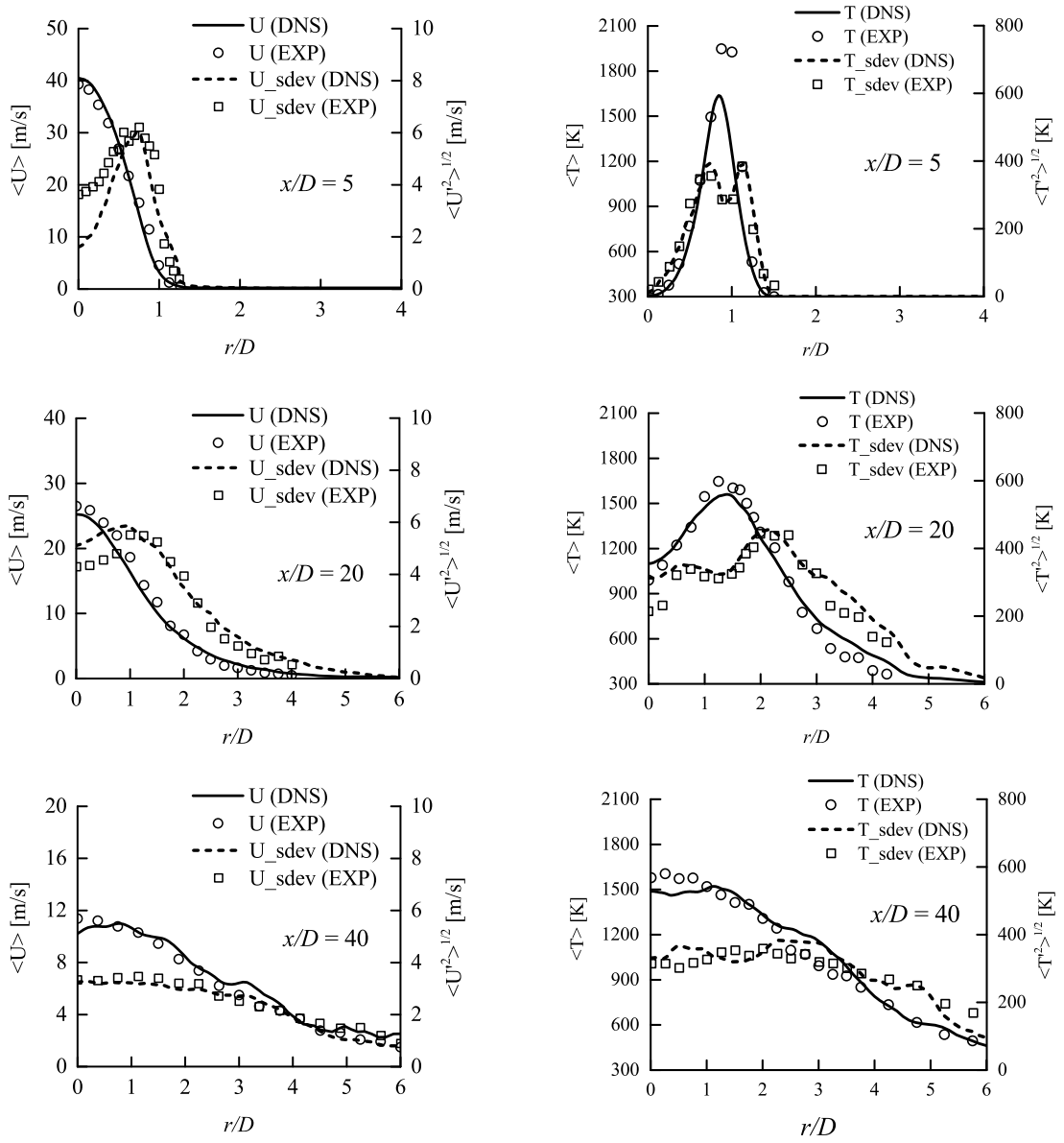

Figure 7: Computed and measured [43] radial profiles of the H3 flame at various streamwise locations. Left column: mean and standard deviation of axial velocity; Right column: mean and standard deviation of temperature. "EXP" stands for experimental data and "sdev" means standard deviation.

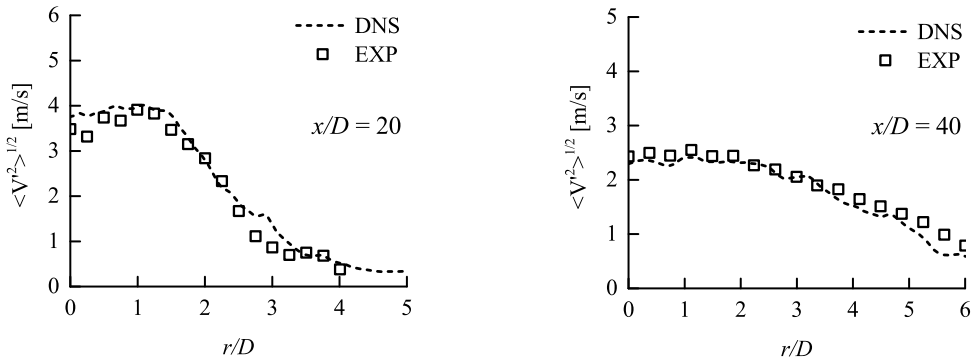

Figure 8: Computed and measured [43] radial profiles of standard deviation of radial velocity at different stream-wise locations for the H3 flame.

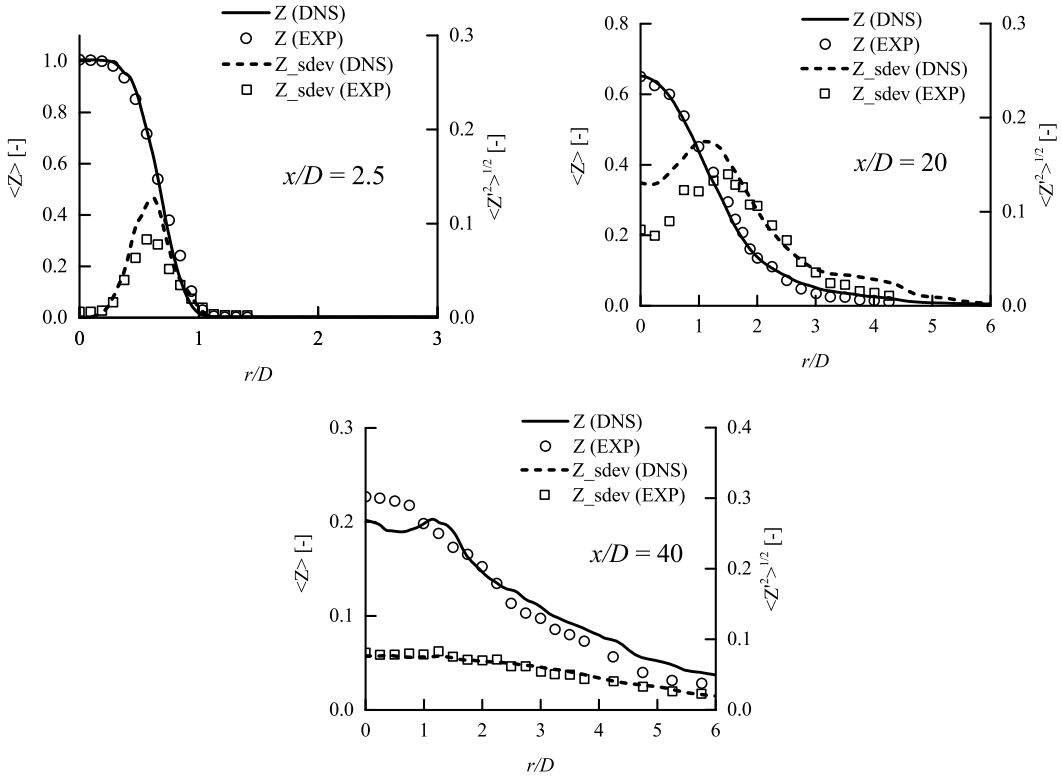

Figure 9: Radial profiles of mean and standard deviation of mixture fraction Z of the H3 flame compared with measurements [43] at different stream-wise locations.

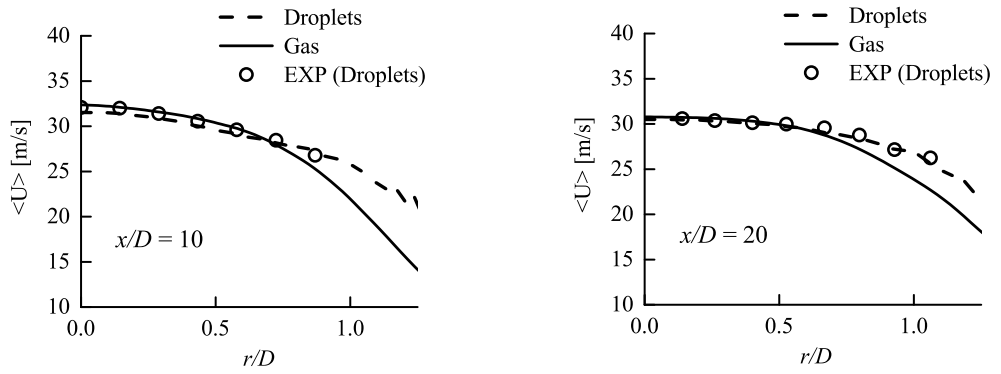

Figure 10: Radial profiles of droplet averaged axial velocity and gas-phase mean axial velocity of spray flame EtF3 compared with measurements [45].

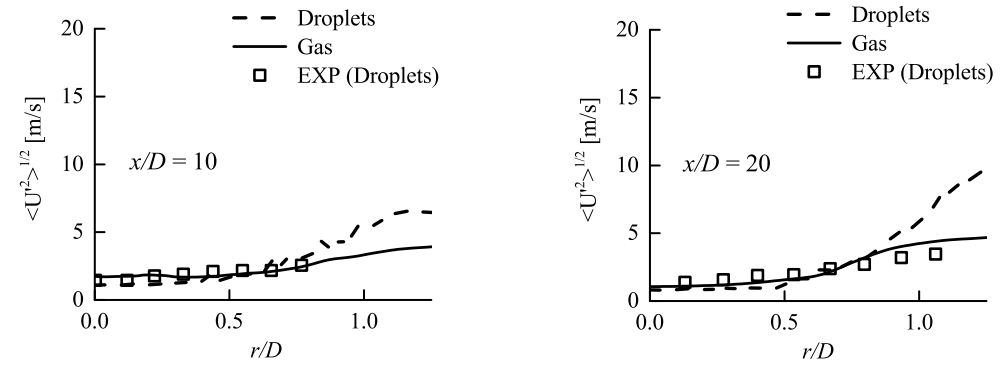

Figure 11: Radial profiles of standard deviation of axial velocity of droplets and gas-phase compared with measurements [45] for spray flame EtF3.

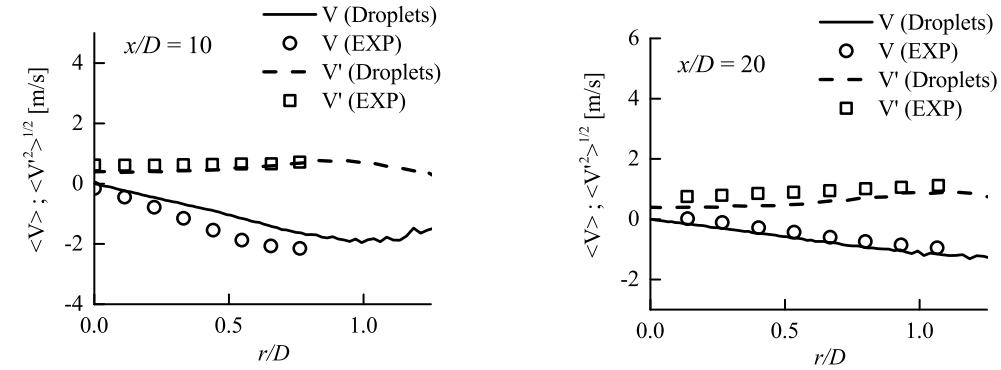

Figure 12: Radial profiles of droplet averaged radial velocity and corresponding standard deviations of spray flame EtF3 compared with measurements [45].

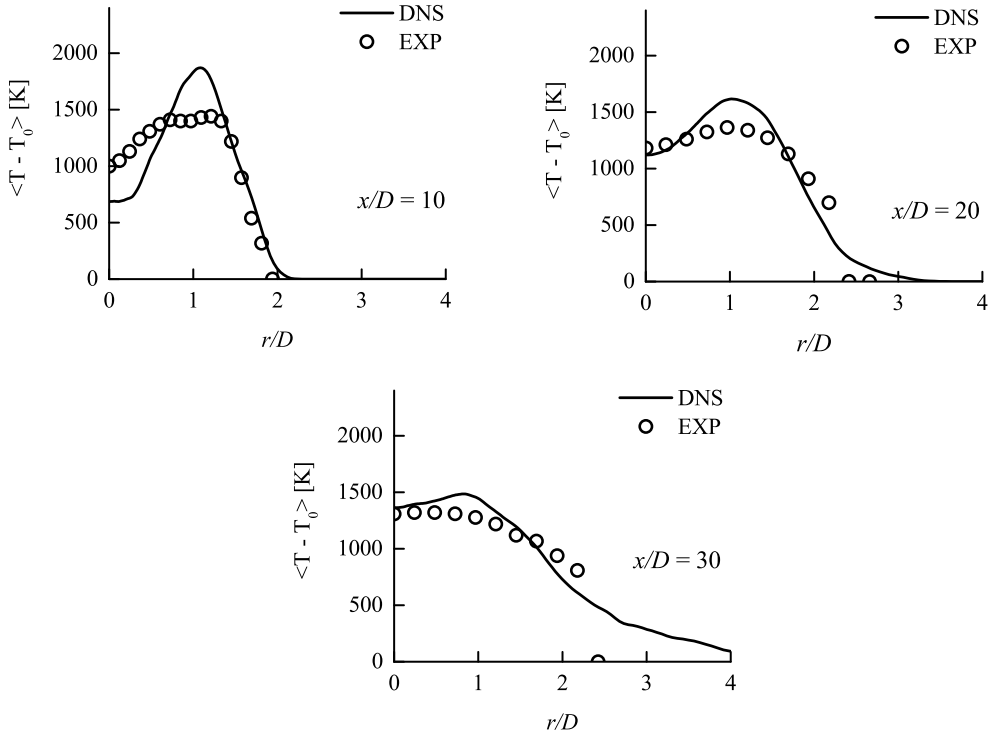

Figure 13: Radial profiles of gas-phase excess temperature of spray flame EtF3 at various stream-wise locations compared with measurements [45]. T_0 is the ambient temperature ($T_0 = 293.15$ K).

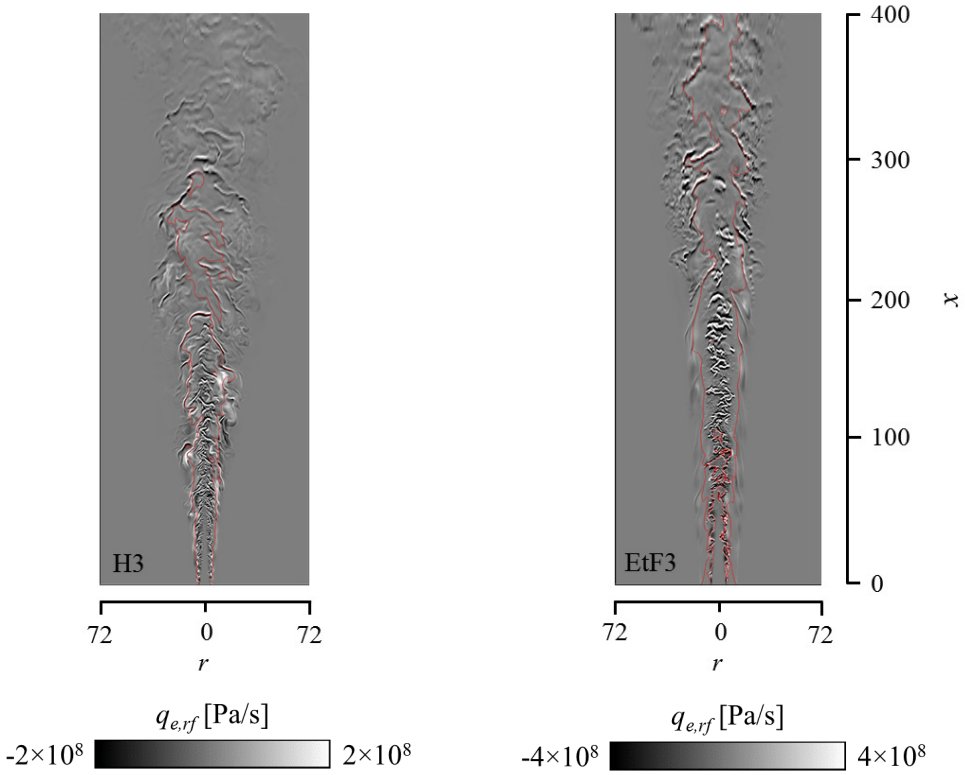

Figure 14: Instantaneous distributions of the acoustic source term $q_{e,rf}$ for the turbulent non-premixed flame H3 (left) and spray flame EtF3 (right). The red lines in each of the instantaneous $q_{e,rf}$ fields represent the iso-surfaces of stoichiometric mixture fraction Z_{st} of the respective flames. Lengths shown in the axial (x) and radial (r) directions are the same for both flames, with all dimensions being in mm.

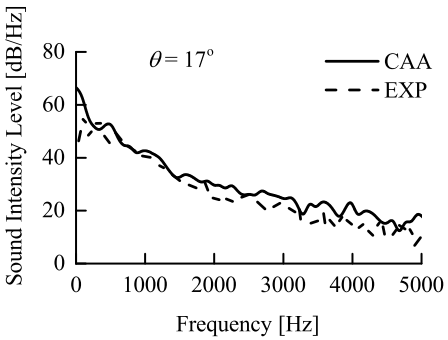

(a) $(x, y) = (640\ \text{mm}, 200\ \text{mm})$; $\theta = 17°$

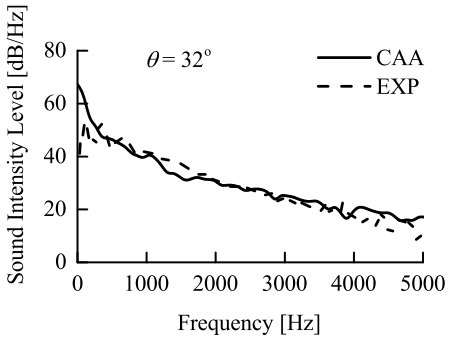

(b) $(x, y) = (640\ \text{mm}, 400\ \text{mm})$; $\theta = 32°$

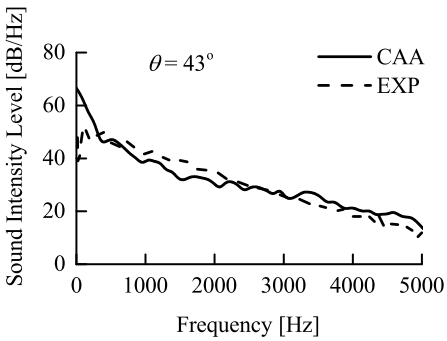

(c) $(x, y) = (544\ \text{mm}, 504\ \text{mm})$; $\theta = 43°$

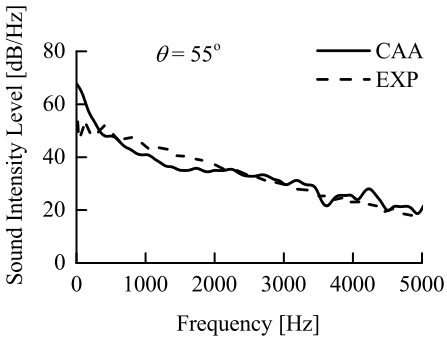

(d) $(x, y) = (344\ \text{mm}, 504\ \text{mm})$; $\theta = 55°$

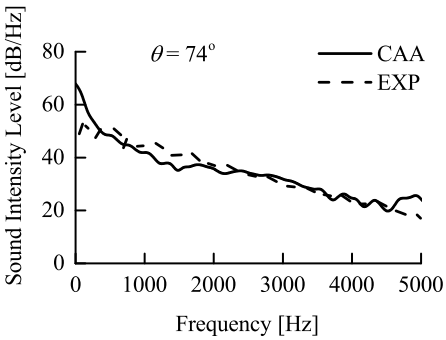

(e) $(x, y) = (144\ \text{mm}, 504\ \text{mm})$; $\theta = 74°$

Figure 15: Computed and measured sound intensity level spectra of H3 flame at various positions. θ is the angle of the observer position with respect to the flame axis.

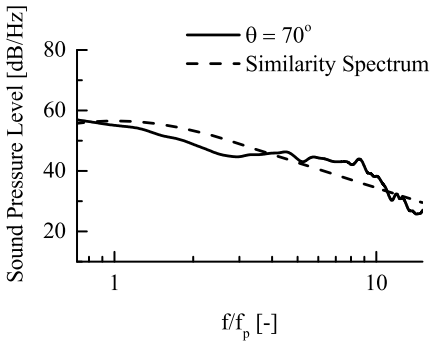

(a) $(x, y) = (144\text{ mm}, 400\text{ mm})$; $\theta = 70°$

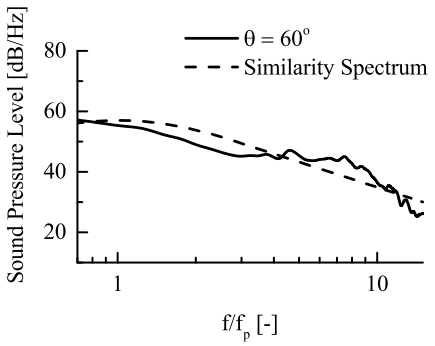

(b) $(x, y) = (240\text{ mm}, 400\text{ mm})$; $\theta = 60°$

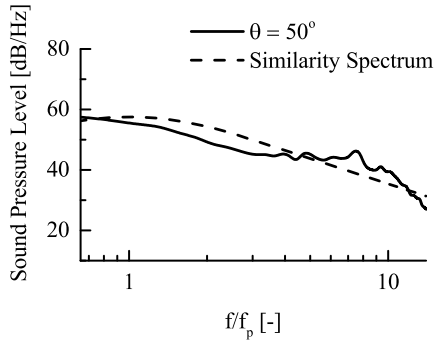

(c) $(x, y) = (336\text{ mm}, 400\text{ mm})$; $\theta = 50°$

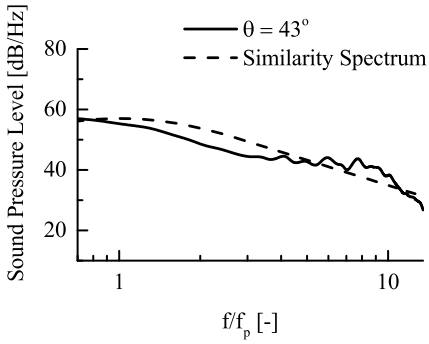

(d) $(x, y) = (432\text{ mm}, 400\text{ mm})$; $\theta = 43°$

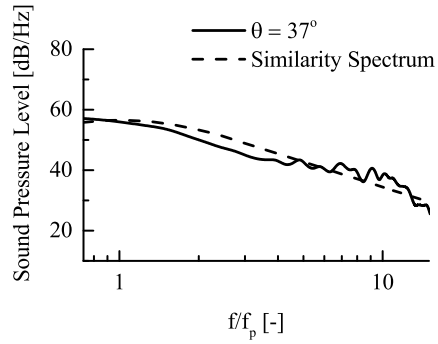

(e) $(x, y) = (528\text{ mm}, 400\text{ mm})$; $\theta = 37°$

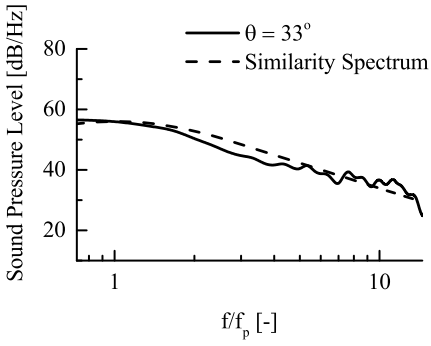

(f) $(x, y) = (624\text{ mm}, 400\text{ mm})$; $\theta = 33°$

Figure 16: Comparison between computed sound pressure spectra of the spray flame EtF3 and the combustion noise similarity spectrum proposed by Tam et al. [98], at various positions that correspond to different radiation angles θ with respect to the flame axis.

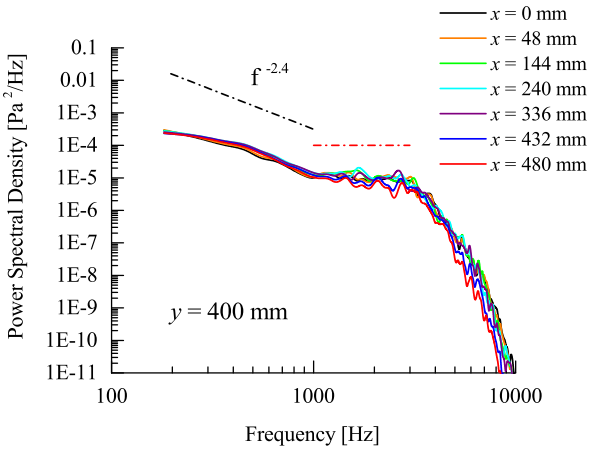

(a)

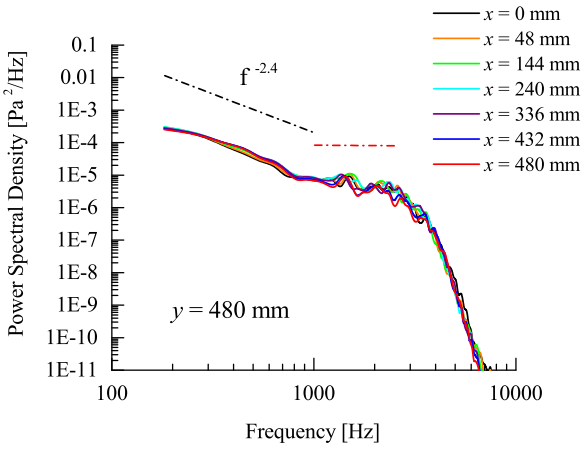

(b)

Figure 17: Acoustic power spectra computed for positions at various stream-wise locations (given by x) from the burner exit, and at a fixed radial distance of (a) $y = 400$ mm and (b) $y = 480$ mm from the flame axis of EtF3 spray flame. The black dash-dotted lines represent the power law dependence $f^{-2.4}$ of the acoustic power spectra. And, the red dash-dotted horizontal lines represent the plateau of nearly constant acoustic power in the computed spectra (discussed later).

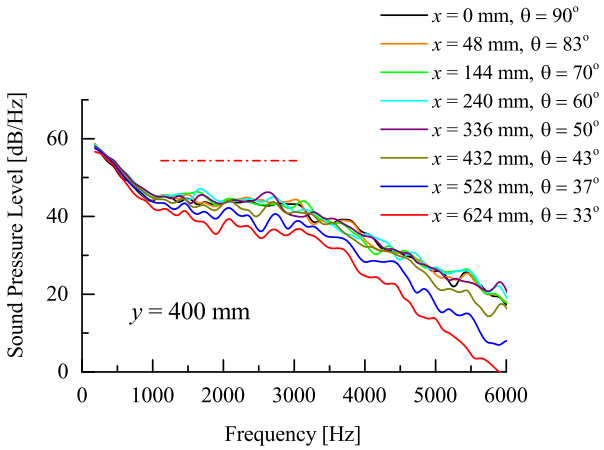

(a)

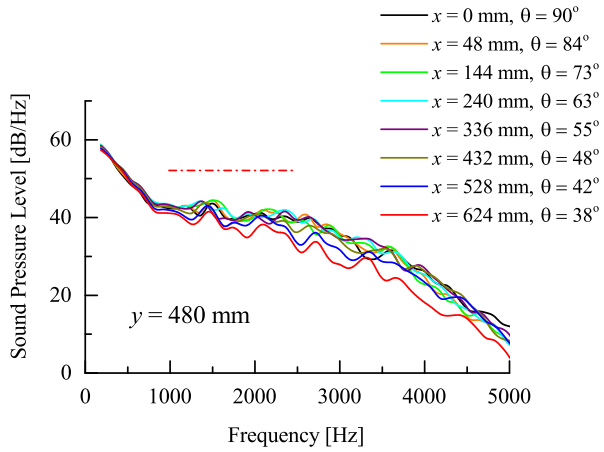

(b)

Figure 18: Sound pressure spectra computed for positions at different stream-wise locations (given by x) from the burner exit, and at a constant radial distance of (a) $y = 400$ mm and (b) $y = 480$ mm from the flame axis of the spray flame EtF3. Each position corresponds to a different radiation angle θ to the flame axis. The red dash-dotted horizontal lines in (a) and (b) qualitatively indicate the constant sound pressure level plateau in the computed spectra.

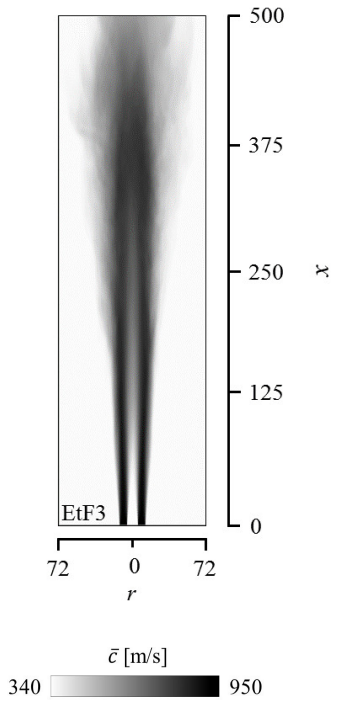

Figure 19: Distribution of the mean speed of sound in the turbulent spray flame EtF3. Dimensions shown in the axial (x) and radial (r) directions are in mm.

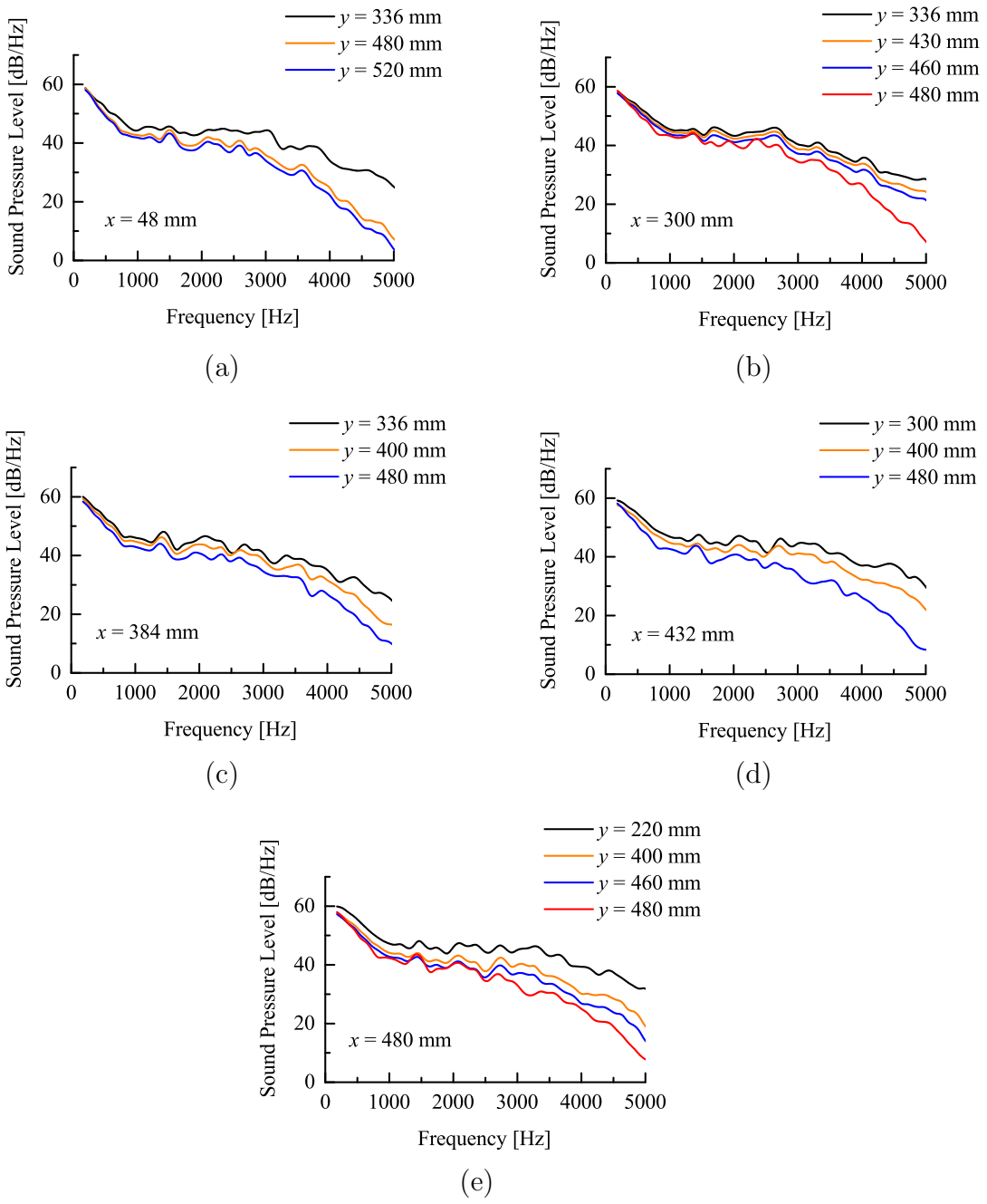

Figure 20: Sound pressure spectra computed for positions at different radial locations (given by y) from the flame axis of the spray flame EtF3, and at fixed axial locations of (a) $x = 48$ mm, (b) $x = 300$ mm, (c) $x = 384$ mm, (d) $x = 432$ mm and (e) $x = 480$ mm from the burner exit.

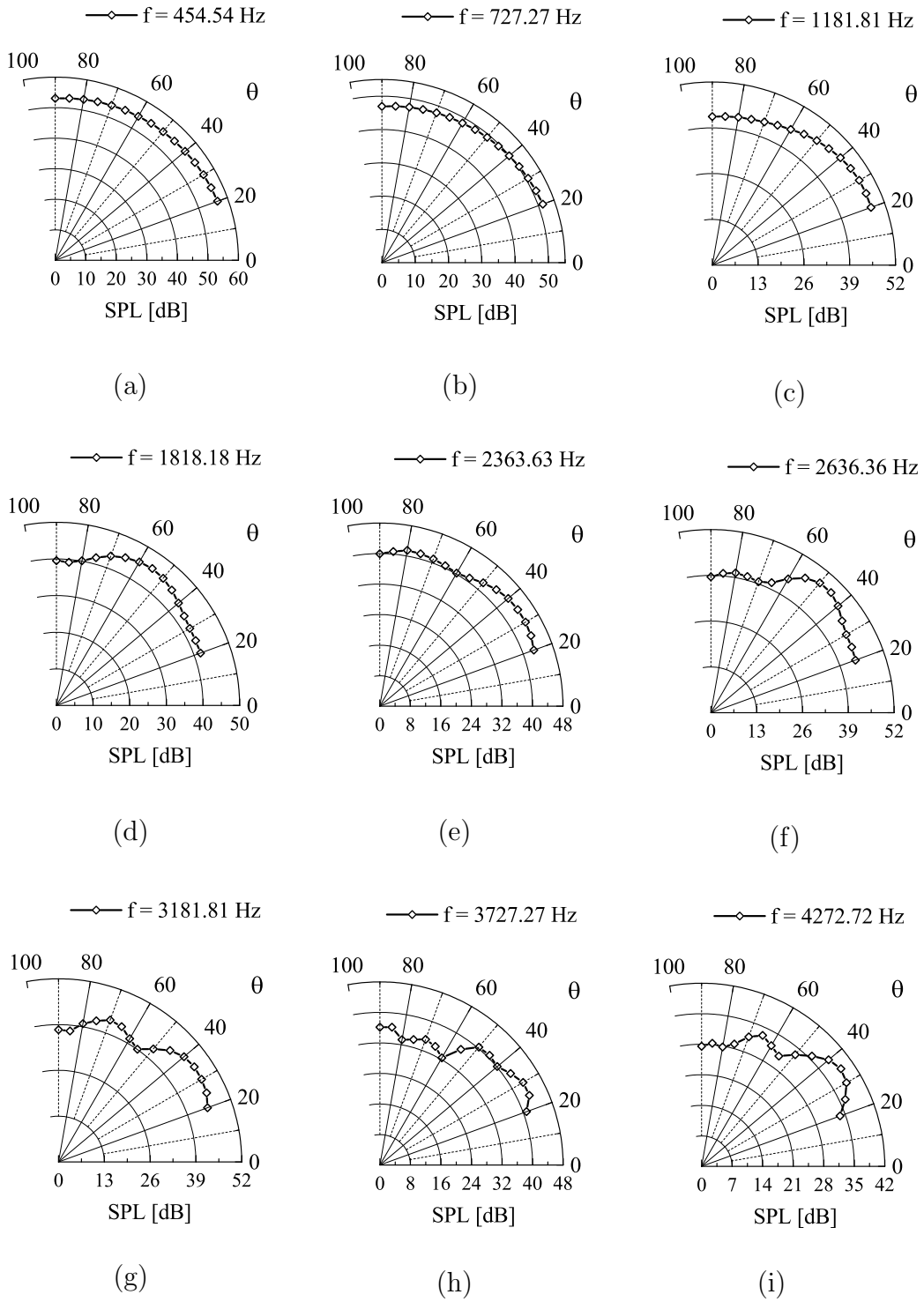
f = 454.54 Hz
f = 727.27 Hz
f = 1181.81 Hz
f = 1818.18 Hz
f = 2363.63 Hz
f = 2636.36 Hz
f = 3181.81 Hz
f = 3727.27 Hz
f = 4272.72 Hz
θ
SPL [dB]
(a)
(b)
(c)
(d)
(e)
(f)
(g)
(h)
(i)

Figure 21:

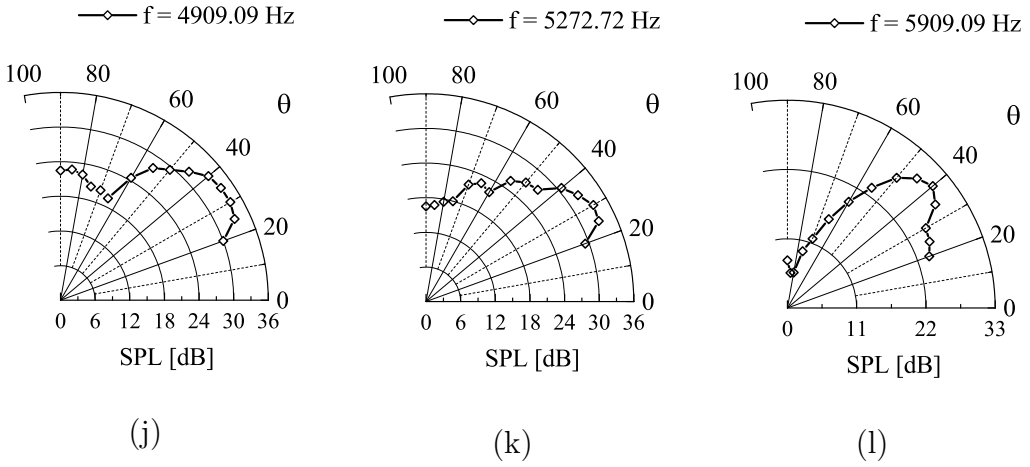

Figure 21: Frequency specific Sound Pressure Level (SPL) computed at various positions on a circular arc of radius $R = 525$ mm in the central x-y plane of the CAA grid, the origin of which is located at the nozzle exit i.e. $(x,y,z) = (0,0,0)$. Each position on this circular arc is considered at an increment of 5 degrees, starting from 20° up to 90° to the flame axis.